ARTICLE

doi:10.1038/nature21388

Autophagy maintains the metabolism and function of young and old stem cells

Theodore T. Ho[1], Matthew R. Warr[1], Emmalee R. Adelman[2], Olivia M. Lansinger[1], Johanna Flach[1], Evgenia V. Verovskaya[1], Maria E. Figueroa[2]† & Emmanuelle Passegué[1]†

With age, haematopoietic stem cells lose their ability to regenerate the blood system, and promote disease development. Autophagy is associated with health and longevity, and is critical for protecting haematopoietic stem cells from metabolic stress. Here we show that loss of autophagy in haematopoietic stem cells causes accumulation of mitochondria and an activated metabolic state, which drives accelerated myeloid differentiation mainly through epigenetic deregulations, and impairs haematopoietic stem-cell self-renewal activity and regenerative potential. Strikingly, most haematopoietic stem cells in aged mice share these altered metabolic and functional features. However, approximately one-third of aged haematopoietic stem cells exhibit high autophagy levels and maintain a low metabolic state with robust long-term regeneration potential similar to healthy young haematopoietic stem cells. Our results demonstrate that autophagy actively suppresses haematopoietic stem-cell metabolism by clearing active, healthy mitochondria to maintain quiescence and stemness, and becomes increasingly necessary with age to preserve the regenerative capacity of old haematopoietic stem cells.

Ageing is the greatest risk factor for many pathological conditions including cancers, neurodegenerative disorders, cardiovascular diseases, and diabetes[1]. Physiological ageing is a complex and multifactorial process that is regulated by both genetic and environmental factors[2]. Although tissues across the body are seemingly affected in different ways, one emerging hallmark of ageing is that reduction in tissue function usually correlates with a reduction in stem cell activity[3]. The blood system is critical for many aspects of organismal health, and proper maintenance of blood production relies on the ability of haematopoietic stem cells (HSCs) to self-renew and differentiate into all lineages of mature blood cells[4]. In adults, HSCs are rare and reside in specialized niches in the bone marrow cavity, where they are kept in a low metabolic, mainly glycolytic, quiescent state unless called upon to regenerate the blood system[5]. With age, HSCs lose their regenerative abilities, but their overall expansion maintains blood production in old organisms, albeit with typical features of blood ageing such as anaemia, immunosenescence, increased production of myeloid cells, and higher predisposition to haematological cancers[6]. Yet, how old HSCs (oHSCs) retain some functional abilities in an adverse ageing bone marrow microenvironment[7,8] remains largely unknown.

Macroautophagy (hereafter called autophagy) is an essential proteostasis and stress response mechanism that maintains cellular health by regulating the quantity and quality of organelles and macromolecules through lysosomal degradation, which is activated in response to nutrient deprivation and other stressors to generate energy and allow survival[9]. Autophagy is controlled by a series of autophagy-related genes (*Atg*) such as the ATG12 conjugation system (*Atg12–Atg5–Atg16*) that are essential for the formation of double-membrane autophagosomes. Autophagy is regulated by important nutrient-sensing pathways including the mechanistic target of rapamycin (mTOR) and 5′ AMP-activated protein kinase (AMPK), which inhibits and activates autophagy, respectively. Autophagy is critical for the proper development of the blood system[10,11], for HSC mobilization[12], and to allow adult HSCs to survive acute metabolic stress[13]. Autophagy declines with age in many tissues[14], and reduced autophagy levels in muscle stem cells directly contribute to decreased regenerative potential and muscle atrophy[15]. In contrast, we previously found increased basal autophagy in oHSCs[13]. Here, we set out to identify how autophagy controls HSC function, and how changes in autophagy levels affect HSC ageing.

Ageing phenotypes upon loss of autophagy

To inactivate autophagy in adult HSCs, we used our previously described *Atg12*$^{flox/flox}$*:Mx1-Cre* conditional knockout (*Atg12*^{cKO}) mouse model[13], and deleted *Atg12* with poly(I:C) (pIC) at 4 weeks of age (Fig. 1a). Surprisingly, the blood system of *Atg12*^{cKO} mice remained largely healthy, with no persisting anaemia or lymphopenia observed over time as reported in other contexts[10,11,16] (Extended Data Fig. 1a). *Atg12*^{cKO} mice showed increased cellularity in the peripheral blood and spleen, and, similar to autophagy inactivation in fetal HSCs[11], had a skewed ratio of circulating myeloid versus lymphoid cells, thus resembling the myeloid-bias observed in old mice (Fig. 1b and Extended Data Fig. 1b–f). In contrast, *Atg12*^{cKO} mice maintained normal numbers of phenotypic HSCs (Lin$^-$/c-Kit$^+$/Sca-1$^+$/Flk2$^-$/CD48$^-$/CD150$^+$) over time, with expanded multipotent progenitor (MPP) and granulocyte/macrophage progenitor (GMP) compartments contributing to the myeloid expansion (Extended Data Fig. 1g–k). These phenotypes were conserved in a distinct *Atg5*$^{flox/flox}$*:Mx1-Cre* conditional knockout (*Atg5*^{cKO}) model (Extended Data Fig. 2a–e), and demonstrated features of premature blood ageing in adult autophagy-deficient mice.

To investigate the regenerative capacity of *Atg12*^{cKO} HSCs, we first performed classic transplantation experiments with purified HSCs to directly measure their self-renewal and multilineage reconstitution activity (Extended Data Fig. 2f). Transplantation of 250 *Atg12*^{cKO} HSCs into lethally irradiated recipients led to significantly impaired engraftment, with reduced overall chimaerism, myeloid-biased lineage distribution, and decreased numbers of regenerated HSCs (Fig. 1c).

[1]Department of Medicine, Hem/Onc Division, The Eli and Edythe Broad Center for Regenerative Medicine and Stem Cell Research, University of California San Francisco, San Francisco, California 94143, USA. [2]Department of Pathology, University of Michigan School of Medicine, Ann Arbor, Michigan 48109, USA. †Present addresses: Department of Human Genetics, Sylvester Comprehensive Cancer Center, University of Miami Miller School of Medicine, Miami, Florida 33136, USA (M.E.F.); Department of Genetics and Development, Columbia Stem Cell Initiative, Columbia University School of Medicine, New York, New York 10032, USA (E.P.).

© 2017 Macmillan Publishers Limited, part of Springer Nature. All rights reserved.

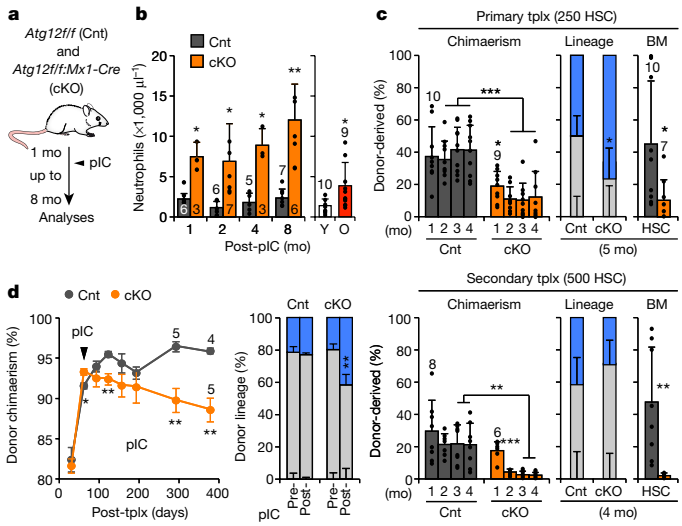

Figure 1 | Accelerated blood ageing phenotypes in autophagy-deficient mice. a, Scheme for deleting *Atg12* in the adult blood system. **b**, Neutrophil counts in peripheral blood of control (Cnt) and $Atg12^{cKO}$ (cKO) mice after pIC (left), and young (Y) and old (O) mice (right); mo, months. **c**, Serial transplantations (tplx) of control and cKO HSCs showing donor chimaerism (left) and lineage distribution (centre) in peripheral blood, and HSC chimaerism (right; BM, bone marrow) at the indicated times after transplantation in primary (top) and secondary (bottom) recipients. **d**, *Atg12* deletion in recipients transplanted with 2×10^6 bone marrow cells from 2-month-old non-pIC-treated control and cKO donors showing donor chimaerism in peripheral blood after pIC (left; ± s.e.m.) and lineage distribution at 61 days (pre-pIC) and 291 days (after pIC) after transplantation (right). Data are mean ± s.d. except when indicated. $*P \leq 0.05$, $**P \leq 0.01$, $***P \leq 0.001$.

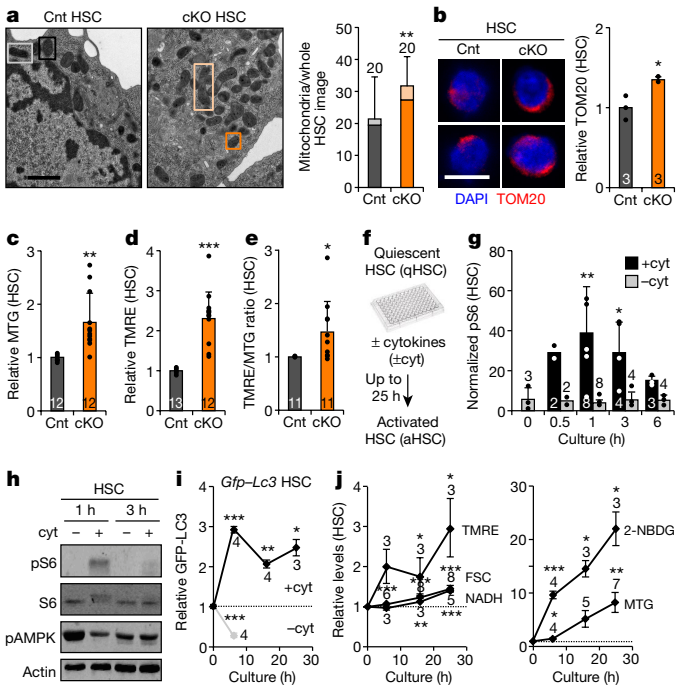

Figure 2 | Mitochondrial characteristics in autophagy-deficient HSCs and activated HSCs. a, Representative electron micrographs and quantification of total, normal (dark box) and elongated (light box) mitochondria in control and cKO HSCs; scale bar, 1 μm. Statistical significance is for all three parameters; *n* indicates cell numbers. **b**, Representative TOM20 immunofluorescence staining and quantification of mitochondria in control and cKO HSCs. **c**–**e**, Mitochondria parameters in control and cKO HSCs: (**c**) MTG levels; (**d**) TMRE levels; and (**e**) TMRE/MTG ratio. **f**–**j**, *In vitro* HSC activation: (**f**) experimental scheme; (**g**) pS6 levels measured by flow cytometry (results are normalized to immunoglobulin-G (IgG) levels); (**h**) pS6, total S6, and pAMPK levels measured by western blot (actin was used as loading control); (**i**) GFP–LC3 levels ($n = 6$ for 0 h; ± s.e.m.); and (**j**) mitochondrial parameters ($n = 6$ (TMRE), 10 (forward scatter, FSC), 7 (NADH), 4 (2-NBDG), and 7 (MTG) at 0 h; ± s.e.m.). Data are mean ± s.d. except when indicated, and are expressed relative to control HSC (**a**–**e**) or 0 h HSC (**g**, **i**, **j**) levels. $*P \leq 0.05$, $**P \leq 0.01$, $***P \leq 0.001$.

These features were further exacerbated upon secondary transplantation of 500 re-isolated $Atg12^{cKO}$ HSCs, and directly demonstrated defective self-renewal activity in autophagy-deficient HSCs that closely resembled the functional impairment of oHSCs (Extended Data Fig. 2g). To address whether the need for autophagy changed with age, we next transplanted 2×10^6 bone marrow cells from non-pIC-treated animals into lethally irradiated mice, induced *Atg12* deletion 2 months after transplantation, and followed the recipients for up to 16 months after pIC treatment (Extended Data Fig. 2h). Of note, $Atg12^{cKO}$ mice could not be aged past 8 months after pIC owing to hepatomegaly from off-target deletion in the liver. Importantly, haematopoietic-specific deletion of *Atg12* in transplanted mice led to a progressive age-related decline in donor-chimaerism and myeloid-biased lineage distribution (Fig. 1d), thus confirming the cell-intrinsic nature of these defects. These ageing features were further exacerbated upon deletion of autophagy in mice transplanted with bone marrow cells from 24-month-old animals (Extended Data Fig. 2i). Collectively, these results indicate striking similarities between autophagy-deficient HSCs and oHSCs with defective self-renewal activity and myeloid-biased differentiation potential, and demonstrate that autophagy is most critical for HSC function during ageing and in conditions of intense regenerative stress such as transplantation.

Autophagy regulates HSC metabolism

We next investigated how loss of autophagy affects HSC function. Electron microscopy analyses revealed increased numbers of total and elongated, fused mitochondria in $Atg12^{cKO}$ HSCs, which was directly confirmed by immunofluorescence staining for the mitochondrial protein TOM20 and flow cytometry measurements of mitochondrial mass with Mitotracker Green (MTG) (Fig. 2a–c and Extended Data Fig. 3a). $Atg12^{cKO}$ HSCs also had expanded endoplasmic reticulum (ER) and Golgi compartments, and increased numbers of small vesicles and lysosomes, confirmed by immunofluorescence staining and flow cytometry dye measurements (Extended Data Fig. 3b–e). These cellular features, together with elevated levels of p62 (Extended Data Fig. 3f), confirmed the loss of bulk autophagy in $Atg12^{cKO}$ HSCs, and suggest activation of alternative mechanisms of cellular recycling[17] to allow HSC maintenance at steady state. Autophagy is known to degrade mitochondria through several pathways including the PINK1/PARK2 stress mitophagy pathway[18], which specifically clears damaged mitochondria. HSCs from $Park2^{-/-}$ mice[19] showed decreased levels of mitochondrial membrane potential dye tetramethylrhodamine-ethyl-ester (TMRE), and TMRE/MTG ratio, probably reflecting damaged mitochondria (Extended Data Fig. 3g). In contrast, $Atg12^{cKO}$ HSCs had increased TMRE levels and TMRE/MTG ratio, indicating more active mitochondria (Fig. 2d, e). Further characterization of $Park2^{-/-}$ mice also revealed no similarities to the phenotypes of $Atg12^{cKO}$ mice, and normal function of $Park2^{-/-}$ HSCs in transplantation experiments (Extended Data Fig. 3h–n). These results indicate that autophagy is most important for the clearance of healthy, active mitochondria in HSCs, as opposed to stress-induced specific removal of damaged mitochondria via mitophagy as recently studied[20,21].

To understand the link between autophagy regulation and mitochondrial activity, we next grew wild-type HSCs or HSCs isolated from autophagy-reporter *Gfp–Lc3* mice[22] in cytokine-rich (+cyt) conditions to force them out of quiescence and investigate their activated state before their first cell division (Fig. 2f). As expected, mTOR was rapidly activated in +cyt conditions, whereas it remained

© 2017 Macmillan Publishers Limited, part of Springer Nature. All rights reserved.

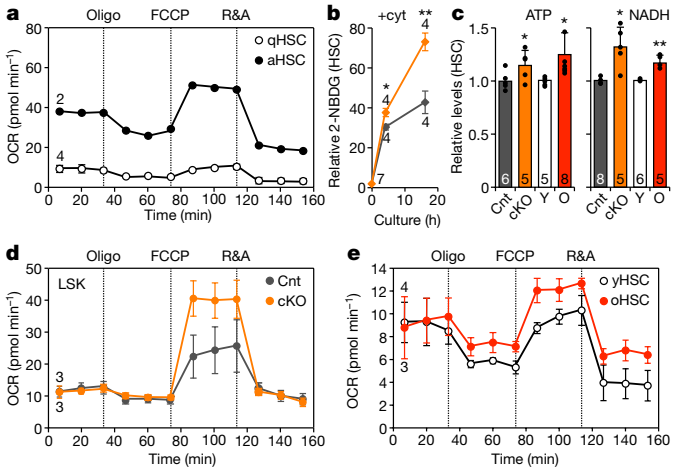

Figure 3 | Loss of autophagy and ageing cause metabolic activation in HSCs. a, OXPHOS levels measured by oxygen consumption rates (OCR) in freshly isolated qHSCs (same as yHSC in **e**) or aHSCs (aHSC; 21 h +cyt culture); oligo, oligomycin; R&A, rotenone and antimycin. **b**, Glucose uptake in control and cKO HSCs cultured as indicated. Results are expressed relative to 0 h control HSC levels. **c**, ATP and NADH levels in the indicated HSC populations (± s.d.). **d**, OXPHOS levels in control and cKO LSK cells. **e**, OXPHOS levels in yHSCs and oHSCs. Data are mean ± s.e.m. except when indicated. $*P \leq 0.05$, $**P \leq 0.01$, $***P \leq 0.001$.

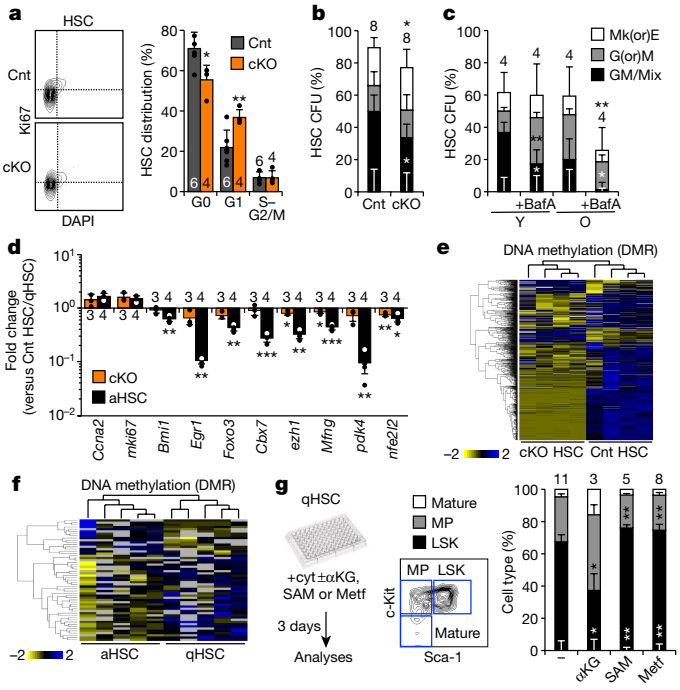

Figure 4 | Loss of autophagy affects HSC fate through epigenetic deregulation. a, Representative flow cytometry plots and quantification of cell cycle distribution in control and cKO HSCs. **b**, **c**, Colony formation in methylcellulose from (**b**) control and cKO HSCs, and (**c**) yHSCs and oHSCs ± BafA; CFU, colony-forming unit; Mk(or)E and G(or)M: mature megakaryocyte, erythroid, granulocyte or macrophage colonies; GM/Mix: immature GM or GMMkE colonies. Results are expressed as percentage of plated cells. **d**, Selected genes from Fluidigm analyses of cKO HSCs and aHSCs. Results are expressed as fold change compared with levels in control HSCs and qHSCs, respectively (3 technical pools of 100 cells are averaged per biological replicate). **e**, **f**, Heatmap of DMRs in (**e**) cKO versus control HSCs ($n = 4$) and (**f**) aHSCs versus qHSCs ($n = 5$) ERRBS analyses. **g**, Impact of αKG, SAM, and metformin (Metf) on HSC differentiation with scheme for *in vitro* treatment (left), gating strategy (middle), and quantification after culture for 3 days. Data are mean ± s.d. $*P \leq 0.05$, $**P \leq 0.01$, $***P \leq 0.001$.

inactive in cytokine-starved (−cyt) conditions, while AMPK was transiently induced (Fig. 2g, h and Extended Data Fig. 4a). This was accompanied by a rapid reduction of GFP–LC3 levels reflecting autophagy activation in –cyt conditions, and increased GFP–LC3 and p62 levels indicating autophagy inhibition in +cyt conditions (Fig. 2i and Extended Data Fig. 4b, c). Furthermore, pharmacological mTOR inhibition or AMPK activation directly induced autophagy in *Gfp–Lc3* HSCs grown in +cyt conditions, while AMPK inhibition reduced autophagy induction in −cyt conditions (Extended Data Fig. 4d). In +cyt conditions, we also found a steady increase in mitochondrial mass and membrane potential, reflecting mitochondrial activation, and cell size, NADH levels and glucose uptake, suggesting increased metabolic activity (Fig. 2j). Seahorse metabolic flux analyses measuring oxygen consumption rates confirmed markedly increased oxidative phosphorylation (OXPHOS) levels in activated HSCs (aHSCs) grown for 21 h in +cyt conditions compared with freshly isolated, quiescent HSCs (qHSCs) (Fig. 3a). Collectively, these results demonstrate that qHSCs switch from a normally low OXPHOS state to a high mitochondria-driven OXPHOS state during activation.

Strikingly, *Atg12*^{cKO} HSCs also exhibited these features of an aHSC state, with increased cell size, NADH, ATP, and glucose uptake (Fig. 3b, c and Extended Data Fig. 4e). Furthermore, freshly isolated HSC-enriched *Atg12*^{cKO} LSK cells (Lin$^-$/c-Kit$^+$/Sca-1$^+$) displayed increased OXPHOS levels, specifically maximum capacity, with unchanged glycolysis levels measured by extracellular acidification rate (Fig. 3d and Extended Data Fig. 4f). Similar to *Atg12*^{cKO} LSKs, oHSCs also exhibited increased cell size, NADH and ATP levels, and elevated OXPHOS with decreased glycolysis (Fig. 3c, e and Extended Data Fig. 4e, g), suggesting an overactive oxidative metabolism. However, in contrast to *Atg12*^{cKO} HSCs, oHSCs had decreased TMRE levels and TMRE/MTG ratios (Extended Data Fig. 4h), which could indicate the presence of some damaged mitochondria[23]. Collectively, these results demonstrate that HSC activation is directly associated with metabolic activation and increased mitochondrial OXPHOS, and that, in the absence of autophagy, HSCs are kept in an activated state reminiscent of the alert state recently described for muscle stem cells[24]. They also show that oHSCs, like autophagy-deficient HSCs, are metabolically more active than young HSCs (yHSC).

Loss of autophagy alters HSC fate

We then explored the consequences of increased oxidative metabolism for *Atg12*^{cKO} HSC fate decisions. Similar to aHSCs, *Atg12*^{cKO} HSCs showed increased levels of reactive oxygen species (ROS), which did not cause DNA damage or apoptosis (Extended Data Figs 4i–k and 5a). As expected for more metabolically activated cells, *Atg12*^{cKO} HSCs also had elevated protein synthesis rates and increased cell cycle activity (Extended Data Fig. 5b, c). Notably, oHSCs showed reduced ROS levels and decreased protein synthesis rates, which contrasted with their OXPHOS-activated status, but is probably influenced by their replication stress features[25] (Extended Data Fig. 5d, e). However, both *Atg12*^{cKO} HSCs and oHSCs[25] displayed a similar loss of quiescence and pro-myeloid differentiation associated with increased unipotent mature colonies and decreased multipotent immature colonies formed in methylcellulose (Fig. 4a, b). Strikingly, yHSCs treated with the autophagy inhibitor bafilomycin A (BafA) and untreated oHSCs showed a matching reduction in multipotent colonies, which was greatly exacerbated in BafA-treated oHSCs (Fig. 4c). Interestingly, treatment with the antioxidant *N*-acetylcysteine (NAC), which is known to ameliorate many ROS-mediated phenotypes[26], did not rescue the precocious myeloid differentiation of *Atg12*^{cKO} HSCs in methylcellulose, nor limit the myeloid expansion in *Atg12*^{cKO} mice treated *in vivo* (Extended Data Fig. 5f–i). These data demonstrate that the non-cytotoxic increase in ROS levels observed in metabolically activated *Atg12*^{cKO} HSCs has no major role in driving precocious myeloid differentiation in

© 2017 Macmillan Publishers Limited, part of Springer Nature. All rights reserved.

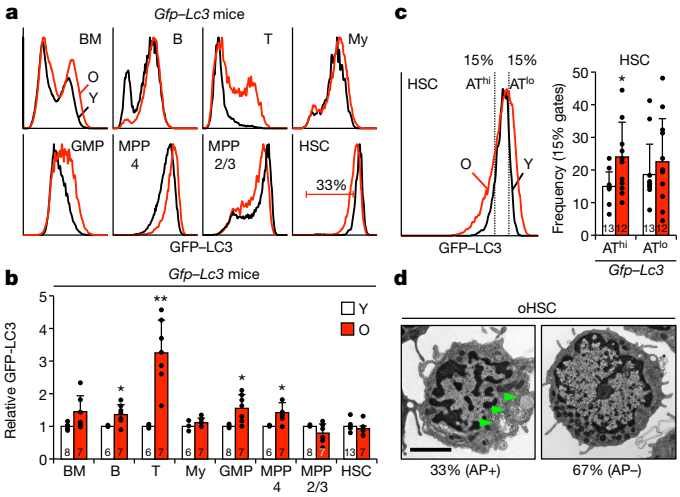

Figure 5 | Different autophagy activity in aged haematopoietic populations. a, **b**, Autophagy levels measured in young and old *Gfp–Lc3* mice: (**a**) representative fluorescence-activated cell sorting (FACS) plots and (**b**) quantification of GFP–LC3 expression. Results are expressed relative to the respective young populations. **c**, Representative FACS plots and frequency of yHSCs and oHSCs within the 15% GFP–LC3 low/autophagy high (AT^{hi}) and 15% GFP–LC3 high/autophagy low (AT^{lo}) yHSC gates. **d**, Representative electron micrographs and percentage of oHSCs ± autophagosomes (AP, arrowheads) (58 cells total); scale bar, 2 μm. Data are mean ± s.d. $*P \leq 0.05$, $**P \leq 0.01$, $***P \leq 0.001$.

autophagy-deficient HSCs, in contrast to what has been shown in myeloid progenitors in flies[27]. Altogether, these results indicate that the overactive metabolic state caused by loss of autophagy results in loss of quiescence and accelerated myeloid differentiation, which closely mirrors the deregulations observed in oHSCs.

Loss of autophagy perturbs HSC epigenetic poising

To gain a better understanding of the mechanisms affected by the loss of autophagy, we performed gene expression microarray analyses on HSCs and GMPs. While significant transcriptional differences were observed in *Atg12*^{cKO} HSCs using a *P* value <0.01, surprisingly, apart from *Atg12*, no individual genes were significantly differentially expressed using a false discovery rate of 0.05 (Supplementary Table 1 and Extended Data Fig. 6a, b). However, gene set enrichment analyses revealed reduced expression of HSC-identity genes[28] and increased expression of both myeloid genes[28] and genes elevated in oHSCs[25] (Extended Data Fig. 6c). Complementary Fluidigm qRT–PCR analyses confirmed limited transcriptional changes in *Atg12*^{cKO} HSCs, but also identified a small set of significantly downregulated genes that render them more similar to downstream MPPs (Fig. 4d and Supplementary Tables 2 and 3). DAVID analyses also showed changes in mitochondrial and other metabolic terms in *Atg12*^{cKO} GMPs, confirming more significant gene expression alterations in progenitor cells (Extended Data Fig. 6d and Supplementary Table 1). Since metabolism has become increasingly linked to epigenetic regulation[26], we also performed enhanced reduced-representation bisulfite sequencing (ERRBS) analyses of DNA methylation. Strikingly, *Atg12*^{cKO} HSCs showed a significantly altered DNA methylation profile, with 162 hypermethylated and 783 hypomethylated differentially methylated regions (DMRs) (Fig. 4e). DAVID analyses identified phosphoproteins as the most enriched class of genes in hypomethylated DMRs (Supplementary Table 4). Taken together, these results are consistent with the idea that changes in fate decisions observed at steady state in autophagy-deficient HSCs are the consequence of an epigenetic reprogramming that begins to alter gene expression in HSCs, with amplification of transcriptional changes in downstream progenitors.

Metabolic-driven epigenetic remodelling

To gain a better understanding of the link between metabolic activation, epigenetic reprograming and control of HSC fate decisions, we conducted a more extensive analysis of 21 h +cyt aHSCs versus freshly isolated qHSCs, and performed both ERRBS and Fluidigm qRT–PCR analyses. Strikingly, we also observed an altered DNA methylation profile, which was more restricted than in *Atg12*^{cKO} HSCs, but also mainly consisted of hypomethylation events with 38 hypomethylated and 17 hyermethylated DMRs (Fig. 4f). Gene Ontology analyses indicated enrichment for Stat3 regulation (Supplementary Table 5). Moreover, we found a clear overlap between the changes in gene expression in aHSCs and *Atg12*^{cKO} HSCs, suggesting activation of similar mechanisms of fate decision (Fig. 4d and Supplementary Table 2). To directly test the importance of metabolic-driven epigenetic remodelling in aHSCs, we added α-ketoglutarate (αKG), a necessary co-factor for many demethylases[29], *S*-adenosylmethionine (SAM), a methyl donor co-substrate for methylases[30], and metformin (Mtf), an inhibitor of mitochondrial complex I[31], to differentiating HSCs grown in +cyt conditions for 3 days, and analysed lineage commitment. Strikingly, addition of αKG enhanced myeloid differentiation, while addition of SAM or Mtf preserved stemness in +cyt HSCs (Fig. 4g). These results indicate that even in the context of strong differentiation stimuli, the epigenetic remodelling associated with metabolic activation directly affects HSC fate decisions. Finally, we measured SAM and αKG cellular levels (Extended Data Fig. 6e, f). While only trending in *Atg12*^{cKO} HSCs, we observed a strong reduction in SAM levels in aHSCs, and found a large increase in αKG levels in both *Atg12*^{cKO} and 21 h +cyt c-Kit-enriched bone marrow cells. These results suggest that epigenetic remodelling and DNA demethylation are early consequences of increased oxidative metabolism, and play a direct role in HSC loss of stemness and accelerated myeloid differentiation. Collectively, they demonstrate an essential role for autophagy in clearing metabolically activated mitochondria and allowing HSCs to maintain a mostly glycolytic, quiescent state.

Autophagy levels define distinct subsets of oHSCs

While oHSCs share many deregulated features with *Atg12*^{cKO} HSCs, we previously reported increased basal autophagy in oHSCs[13]. To address this discrepancy and to determine its significance, we profiled GFP–LC3 expression in various haematopoietic populations of young and old *Gfp–Lc3* mice as a surrogate of autophagy levels. In unfractionated bone marrow cells, mature B and T cells, and most of the progenitor populations including GMPs and MPP4, GFP–LC3 levels were increased with age, indicating an overall decrease in autophagy activity, as already reported for T cells[32] (Fig. 5a, b). Interestingly, this corresponded to populations that were either unchanged or decreased in number in old mice (Extended Data Fig. 7a). In contrast, expanded myeloid cells did not have altered GFP–LC3 levels, and the enlarged MPP2/3 and HSC compartments both contained subsets with decreased GFP–LC3 expression. While the average GFP–LC3 expression and overall mTOR activity did not significantly change between yHSCs and oHSCs (Extended Data Fig. 7b), careful examination of oHSCs revealed an increase in cells with both lower and higher GFP–LC3 levels, reflecting the appearance of subsets with either high autophagy (AT^{hi}) or low autophagy (AT^{lo}), respectively (Fig. 5c). Re-analysis of electron microscopy pictures[13] (Fig. 5d) and measurement of autophagy with Cyto-ID dye (Extended Data Fig. 7c, d) also indicated that approximately one-third of oHSCs had autophagosomes and activated autophagy. Thus, while most of the blood cells including most of the HSC compartment show no activation or a decline in autophagy with age, a fraction of oHSCs have increased autophagy levels.

To study the differences between AT^{hi} and AT^{lo} oHSCs, we isolated cells with the 33% lowest and 33% highest GFP–LC3 levels, respectively (Extended Data Fig. 7e). This sub-fractionation revealed no changes in nuclear FoxO3a, but uncovered decreased mTOR activity specifically in AT^{hi} oHSCs (Fig. 6a and Extended Data Fig. 7f), thus identifying the cause for autophagy induction in this subset. By electron microscopy

© 2017 Macmillan Publishers Limited, part of Springer Nature. All rights reserved.

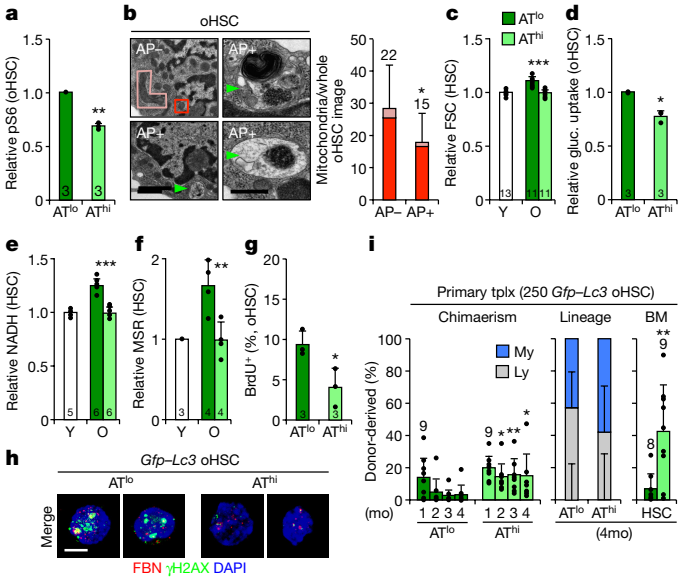

Figure 6 | Autophagy-activated oHSCs are healthier stem cells. **a**, pS6 levels in AT^{lo} and AT^{hi} oHSCs. **b**, Representative electron micrographs and quantification of total, normal (dark box) and elongated (light box) mitochondria in oHSCs ± autophagosomes (AP, arrowheads); scale bars, 1 μm. Statistical significance is for all three parameters; *n* indicates cell numbers. **c**–**f**, Metabolic parameters in AT^{lo} and AT^{hi} oHSCs: (**c**) cell size, (**d**) glucose (gluc.) uptake, (**e**) NADH, and (**f**) ROS levels. **g**, Cycling activity in AT^{lo} and AT^{hi} oHSCs. **h**, Representative examples of three independent experiments showing immunofluorescence images of fibrillarin (FBN)/γH2AX replication stress foci in AT^{lo} and AT^{hi} oHSCs; scale bar, 5 μm. **i**, Transplantation of AT^{lo} and AT^{hi} oHSC subsets with donor chimaerism (left) and lineage distribution (centre) in peripheral blood, and HSC chimaerism (right) at the indicated times in primary recipients. Data are mean ± s.d., and are expressed relative to AT^{lo} oHSCs (**a**, **d**) or yHSCs (**c**, **e**, **f**). $*P \leq 0.05$, $**P \leq 0.01$, $***P \leq 0.001$.

analyses, oHSCs with autophagosomes displayed normal youthful organelle biology, while oHSCs without autophagosomes showed almost identical features to *Atg12*^{cKO} HSCs, with expanded ER, Golgi, and small vesicle compartments, and increased numbers of total and elongated mitochondria, which was confirmed by TOM20 immunofluorescence staining in AT^{lo} oHSCs (Fig. 6b and Extended Data Fig. 7g, h). AT^{lo} oHSCs also had increased cell size and elevated TMRE, NADH, ATP, glucose uptake, and ROS levels (Fig. 6c–f and Extended Data Fig. 7i–k), remarkably similar to the overactive metabolic features of *Atg12*^{cKO} HSCs. This resulted in increased cell cycling, overproliferation in self-renewal conditions, and pro-myeloid differentiation specifically in AT^{lo} oHSCs (Fig. 6g and Extended Data Fig. 7l, m). Strikingly, nucleolar γH2AX foci that are hallmarks of replication stress in oHSCs[25] were almost exclusively found in AT^{lo} oHSCs (Fig. 6h). In contrast, AT^{hi} oHSCs closely resembled healthy yHSCs for all of these characteristics. Taken together, these results indicate that by preventing entry into an activated state, autophagy preserves a subset of oHSCs from replication stress and associated cellular ageing. This is actually very different from the functions of autophagy in muscle stem-cell activation[33] and prevention of senescence[15].

Autophagy activation maintains healthier oHSCs

We next analysed the functionality of these subsets and transplanted 250 AT^{lo} or AT^{hi} oHSCs into lethally irradiated recipients (Extended Data Fig. 8a). While both subsets initially engrafted at similar levels, AT^{lo} oHSCs rapidly declined and were unable to maintain efficient long-term reconstitution and HSC numbers (Fig. 6i). In contrast, AT^{hi} oHSCs exhibited surprisingly robust long-term reconstitution and HSC regeneration potential. These functional differences persisted with a more restrictive 15% GFP–LC3 AT$^{hi/lo}$ oHSC cutoff and upon secondary transplantation, although they became attenuated, perhaps owing to normalization of autophagy levels in re-isolated oHSC subsets, potentially as a consequence of repeated exposure to a young bone marrow microenvironment (Extended Data Fig. 8b, c). They were also specific to oHSCs, as AT^{lo} and AT^{hi} yHSCs isolated with the same 33% GFP–LC3 cutoffs had no differences in regenerative abilities (Extended Data Fig. 8d). Collectively, these results demonstrate that AT^{lo} and AT^{hi} oHSCs are functionally distinct subsets, with autophagy-activated oHSCs being the fittest aged stem cells responsible for the majority of the repopulation potential, and autophagy-inactivated oHSCs driving most of the blood ageing phenotypes.

We also investigated the reversibility between AT^{lo} and AT^{hi} oHSC subsets. Strikingly, there were no discernible differences in CD150 expression between these two subsets, and oHSCs were almost identical to yHSCs for both mTOR activation in +cyt conditions and pharmacological modulation of autophagy levels (Extended Data Fig. 9a–c). In fact, AT^{lo} and AT^{hi} oHSCs, despite initial differences in GFP–LC3 levels, were able to repress and activate autophagy to similar extents in ±cyt conditions, and upon glutamine starvation (Extended Data Fig. 9d–g). Furthermore, both AT^{lo} and AT^{hi} oHSCs had equivalent autophagy flux, which was comparable to yHSCs (Extended Data Fig. 9f). These results demonstrate that while subsets of oHSCs with different mTOR and autophagy levels exist *in vivo*, they both maintain the ability to upregulate and downregulate autophagy upon strong stimulation.

Discussion

Our results demonstrate an essential function for autophagy in removing activated mitochondria and controlling oxidative metabolism, thereby maintaining HSC stemness and regenerative potential (Extended Data Fig. 10). They link metabolic reprogramming with epigenetic modifications in the control of HSC fate, and establish autophagy as one of the essential gatekeepers of HSC quiescence. This role becomes even more important during ageing as the inability of the majority of oHSCs to activate autophagy *in vivo* results in an overactive OXPHOS metabolism that drives most of the ageing blood phenotypes, including impaired engraftment and replication stress. While all oHSCs remain competent for autophagy induction, only about one-third of them activate autophagy in the ageing bone marrow microenvironment[7,8], and maintain a low metabolic state with robust regeneration potential akin to yHSCs. Our findings have exciting implications for rejuvenation therapies as they identify a cellular characteristic that can be directly targeted to improve oHSC function and preserve the health of an ageing blood system. In this context, understanding why some old stem cells activate autophagy and others do not, as well as identifying the environmental drivers for this differential adaptive response, will help further our understanding of cellular ageing, and develop more targeted approaches for improving organismal health during ageing.

Online Content Methods, along with any additional Extended Data display items and Source Data, are available in the online version of the paper; references unique to these sections appear only in the online paper.

Received 23 May 2016; accepted 12 January 2017.
Published online 1 March 2017.

1. Niccoli, T. & Partridge, L. Ageing as a risk factor for disease. *Curr. Biol.* **22,** R741–R752 (2012).
2. Rando, T. A. Stem cells, ageing and the quest for immortality. *Nature* **441,** 1080–1086 (2006).
3. López-Otín, C., Blasco, M. A., Partridge, L., Serrano, M. & Kroemer, G. The hallmarks of aging. *Cell* **153,** 1194–1217 (2013).
4. Orkin, S. H. & Zon, L. I. Hematopoiesis: an evolving paradigm for stem cell biology. *Cell* **132,** 631–644 (2008).
5. Kohli, L. & Passegué, E. Surviving change: the metabolic journey of hematopoietic stem cells. *Trends Cell Biol.* **24,** 479–487 (2014).
6. Geiger, H., de Haan, G. & Florian, M. C. The ageing haematopoietic stem cell compartment. *Nature Rev. Immunol.* **13,** 376–389 (2013).
7. Ergen, A. V., Boles, N. C. & Goodell, M. A. Rantes/Ccl5 influences hematopoietic stem cell subtypes and causes myeloid skewing. *Blood* **119,** 2500–2509 (2012).

© 2017 Macmillan Publishers Limited, part of Springer Nature. All rights reserved.

8. Kusumbe, A. P. *et al.* Age-dependent modulation of vascular niches for haematopoietic stem cells. *Nature* **532,** 380–384 (2016).
9. He, C. & Klionsky, D. J. Regulation mechanisms and signaling pathways of autophagy. *Annu. Rev. Genet.* **43,** 67–93 (2009).
10. Liu, F. *et al.* FIP200 is required for the cell-autonomous maintenance of fetal hematopoietic stem cells. *Blood* **116,** 4806–4814 (2010).
11. Mortensen, M. *et al.* The autophagy protein Atg7 is essential for hematopoietic stem cell maintenance. *J. Exp. Med.* **208,** 455–467 (2011).
12. Leveque-El Mouttie, L. *et al.* Autophagy is required for stem cell mobilization by G-CSF. *Blood* **125,** 2933–2936 (2015).
13. Warr, M. R. *et al.* FOXO3A directs a protective autophagy program in haematopoietic stem cells. *Nature* **494,** 323–327 (2013).
14. Rubinsztein, D. C., Mariño, G. & Kroemer, G. Autophagy and aging. *Cell* **146,** 682–695 (2011).
15. García-Prat, L. *et al.* Autophagy maintains stemness by preventing senescence. *Nature* **529,** 37–42 (2016).
16. Levine, B., Mizushima, N. & Virgin, H. W. Autophagy in immunity and inflammation. *Nature* **469,** 323–335 (2011).
17. Codogno, P., Mehrpour, M. & Proikas-Cezanne, T. Canonical and non-canonical autophagy: variations on a common theme of self-eating? *Nature Rev. Mol. Cell Biol.* **13,** 7–12 (2011).
18. Youle, R. J. & Narendra, D. P. Mechanisms of mitophagy. *Nature Rev. Mol. Cell Biol.* **12,** 9–14 (2011).
19. Goldberg, M. S. *et al.* Parkin-deficient mice exhibit nigrostriatal deficits but not loss of dopaminergic neurons. *J. Biol. Chem.* **278,** 43628–43635 (2003).
20. Vannini, N. *et al.* Specification of haematopoietic stem cell fate via modulation of mitochondrial activity. *Nature Commun.* **7,** 13125 (2016).
21. Ito, K. *et al.* Self-renewal of a purified $Tie2^{+}$ hematopoietic stem cell population relies on mitochondrial clearance. *Science* **354,** 1156–1160 (2016).
22. Mizushima, N., Yamamoto, A., Matsui, M., Yoshimori, T. & Ohsumi, Y. *In vivo* analysis of autophagy in response to nutrient starvation using transgenic mice expressing a fluorescent autophagosome marker. *Mol. Biol. Cell* **15,** 1101–1111 (2004).
23. Mohrin, M. *et al.* Stem cell aging. A mitochondrial UPR-mediated metabolic checkpoint regulates hematopoietic stem cell aging. *Science* **347,** 1374–1377 (2015).
24. Rodgers, J. T. *et al.* mTORC1 controls the adaptive transition of quiescent stem cells from G_0 to G_{Alert}. *Nature* **510,** 393–396 (2014).
25. Flach, J. *et al.* Replication stress is a potent driver of functional decline in ageing haematopoietic stem cells. *Nature* **512,** 198–202 (2014).
26. Chandel, N. S., Jasper, H., Ho, T. T. & Passegué, E. Metabolic regulation of stem cell function in tissue homeostasis and organismal ageing. *Nature Cell Biol.* **18,** 823–832 (2016).
27. Owusu-Ansah, E. & Banerjee, U. Reactive oxygen species prime *Drosophila* haematopoietic progenitors for differentiation. *Nature* **461,** 537–541 (2009).
28. Chambers, S. M. *et al.* Hematopoietic fingerprints: an expression database of stem cells and their progeny. *Cell Stem Cell* **1,** 578–591 (2007).
29. Kohli, R. M. & Zhang, Y. TET enzymes, TDG and the dynamics of DNA demethylation. *Nature* **502,** 472–479 (2013).
30. Fuso, A., Cavallaro, R. A., Orrù, L., Buttarelli, F. R. & Scarpa, S. Gene silencing by *S*-adenosylmethionine in muscle differentiation. *FEBS Lett.* **508,** 337–340 (2001).
31. Owen, M. R., Doran, E. & Halestrap, A. P. Evidence that metformin exerts its anti-diabetic effects through inhibition of complex 1 of the mitochondrial respiratory chain. *Biochem. J.* **348,** 607–614 (2000).
32. Puleston, D. J. *et al.* Autophagy is a critical regulator of memory $CD8^{+}$ T cell formation. *eLife* **3,** e03706 (2014).
33. Tang, A. H. & Rando, T. A. Induction of autophagy supports the bioenergetic demands of quiescent muscle stem cell activation. *EMBO J.* **33,** 2782–2797 (2014).

Supplementary Information is available in the online version of the paper.

Acknowledgements We thank J. Debnath for help with these studies, A. Brunet and S. Villeda for providing some old C57Bl/6 mice, J. Cox and D. Ruggero for the gift of *Park2*$^{-/-}$ mice and Ink128, respectively, S. Y. Zhang for overall assistance, J. Wong for help with Seahorse studies, J. Wong for electron microscopy analyses, J. Pollack for assistance with bioinformatics, P. Nyugen for contribution to confocal imaging, M. Lee for management of the Flow Cytometry Core Facility, and all members of the Passegué laboratory for insights and suggestions. T.T.H. is supported by an AHA Predoctoral Fellowship and T32GM008284, M.R.W by a LLS Special Fellow Award, E.A. by T32AG000114, and E.V. by a Netherlands Organisation for Scientific Research (NWO) Rubicon Fellowship and a BD Biosciences Stem Cell grant. This work was supported by National Institutes of Health R01HL126947 to M.E.F., and National Institutes of Health R01CA184014 and P30DK063720, a Program for Breakthrough Biomedical Research New Frontier Research Award, a Glenn Foundation Research Award, and a Leukemia & Lymphoma Society Scholar Award to E.P.

Author Contributions T.T.H. performed all of the experiments with help from M.R.W. for the initial *Atg12*^{cKO} mice analyses, E.R.A. and M.E.F. for DNA methylation studies, O.M.L. and E.V.V. for technical assistance, and J.F. for *O*-propargyl-puromycin experiments. T.T.H., M.R.W., and E.P. designed the experiments and interpreted the results. T.T.H. and E.P. wrote the manuscript.

Author Information Reprints and permissions information is available at www.nature.com/reprints. The authors declare no competing financial interests. Readers are welcome to comment on the online version of the paper. Correspondence and requests for materials should be addressed to E.P. (passeguee@stemcell.ucsf.edu).

© 2017 Macmillan Publishers Limited, part of Springer Nature. All rights reserved.

METHODS

Mice. Young (6–12 weeks) and old (24–28 months) wild-type C57Bl/6 mice of both genders were either bred and aged in house, or obtained from the National Institute on Ageing aged rodent colonies. *Mx1-Cre* (ref. 34), *Atg12*$^{flox/flox}$*:Mx1-Cre* (ref. 13), *Atg5*$^{flox/flox}$ (ref. 35), *Park2*$^{-/-}$ (ref. 19), and *Gfp–Lc3* (ref. 22) were all on a pure C57Bl/6 background and have been described previously. *Atg5*$^{flox/flox}$*:Mx1-Cre* mice were generated by crossing *Atg5*$^{flox/flox}$ with *Mx1-Cre* mice. Old (24–31 months) *Gfp–Lc3* mice were aged in house. For *Mx1-Cre*-mediated deletion, 4-week-old mice were injected intraperitoneally three times 2 days apart with 125 μg poly(I/C) (pIC, GE Healthcare) in 100 μl PBS. pIC-injected *Atg12*$^{flox/flox}$ or *Atg5*$^{flox/flox}$ mice were used as controls. pIC-injected *Atg12*$^{flox/flox}$*:Mx1-Cre* and *Atg5*$^{flox/flox}$*:Mx1-Cre* conditional knockout (cKO) mice were used 2–3 months after pIC injection, unless otherwise indicated. For deletion in transplanted mice, recipients were injected 2 months after transplantation with pIC as described above. For mouse studies, no specific randomization or blinding protocol was used, animals of both genders were used, and all experiments were performed in accordance with University of California, San Francisco (UCSF) Institutional Animal Care and Use Committee approved protocols.

***In vivo* assays.** For 5-fluorouracil (5-FU; Sigma-Aldrich) treatment, mice were injected intraperitoneally with 150 mg/kg 5-FU or vehicle (PBS) four times once a month and analysed for blood parameters by regular bleeding every 3–5 days. For *in vivo* starvation experiments, mice were deprived of food for 24 h with free access to water. For transplantations experiments, 8- to 12-week-old CD45.1 C57Bl/6-Boy/J recipient mice were lethally irradiated (11 Gy, delivered in split doses 3 h apart) using a ^{137}Cs source (J. L. Shepherd), and injected retro-orbitally with either 250–1,000 purified CD45.2 HSCs delivered together with 250,000 Sca-1-depleted helper CD45.1 bone marrow cells or just with 2×10^6 unfractionated CD45.2 bone marrow cells. Transplanted mice were kept on antibiotic-containing water for 4 weeks, and analysed for donor-derived chimaerism by monthly bleeding. Peripheral blood was obtained via retro-orbital bleeding, and collected in 4 ml of ACK (150 mM NH_4Cl/10 mM $KHCO_3$) containing 10 mM EDTA for flow cytometry analyses, or in EDTA-coated tubes (Becton Dickinson) for complete blood counts. Complete blood count analyses were performed using a Hemavet haematology system (Drew Scientific). For EdU incorporation, mice were injected with 100 μl of 1 mg/ml 5-ethynyl-2 deoxyuridine (EdU, Thermo Fisher Scientific, A00144) 3 h before being killed. For NAC treatments, mice were given water containing 1 mg/ml NAC (Sigma-Aldrich, A7250-100G) for 8 weeks starting on the day of the final pIC treatment.

Flow cytometry. Haematopoietic stem and progenitor cells were analysed and/or isolated as described[36]. Bone marrow cells were obtained by crushing leg, arm, and pelvic bones (with eventually sternum and spines for some experiments) in Hanks' buffered saline solution (HBSS) containing 2% heat-inactivated FBS (staining media), and single-cell suspensions of splenocytes by mechanical dissociation between two slides of whole spleens. Erythrocytes were removed by ACK lysis, and single-cell suspensions of bone marrow cells were purified on a Ficoll gradient (Histopaque 1119, Sigma-Aldrich). Bone marrow cells were then enriched for c-Kit$^+$ cells using c-Kit microbeads (Miltenyi Biotec, 130-091-224) and an AutoMACS cell separator (Miltenyi Biotec) or MACS Separation LS Columns (Miltenyi Biotec, 130-042-401). For cell analyses, unfractionated bone marrow cells were incubated with purified rat anti-mouse lineage antibodies (CD3 from BioLegend, and CD4, CD5, CD8, B220, Ter119, Mac-1, and Gr-1 from eBioscience) followed by goat anti-rat-PE-Cy5 (Invitrogen, A10691) and subsequently blocked with purified rat IgG (Sigma-Aldrich). Cells were then stained with c-Kit-APC-eFluor780 (eBioscience, 47-1171-82), Sca-1-PB (BioLegend, 108120), CD48-A647 (BioLegend, 103416), CD150-PE (BioLegend, 115904), and Flk2-bio (eBioscience, 13-1351-82) followed by either SA-PeCy7 (eBioscience, 25-4317-82) or SA-Qdot605 (Invitrogen, Q10101MP) for HSC staining, or together with CD34-FITC (eBioscience, 11-0341-85) and Fcγ R-PerCP-eFluor710 (eBioscience, 46-0161-82) for combined HSC/myeloid progenitor staining. For *Gfp–Lc3* mice analyses and dye staining requiring FITC and/or PE channels, HSCs were stained instead with Lin/PE-Cy5, Sca-1-PE-Cy7 (BioLegend, 108114), CD48-PB (BioLegend, 1103418), CD150-APC (BioLegend, 1115910), and Flk2-Bio followed by SA-PeCy7. For myeloid progenitor analyses in *Gfp–Lc3* mice, cells were separately stained with Lin/PE-Cy5, c-Kit-APC-eFluor780, Sca-1-PB, Fcγ R-PerCP-eFluor710, and CD34-Bio (BioLegend, 119304) followed by SA-Qdot605. For HSC chimaerism analyses, HSCs were stained with Lin/PE-Cy5, c-Kit-APC-eFluor780, Sca-1-PB, CD48-A647, CD150-PE, and Flk2-bio followed by SA-Qdot605, together with CD45.2-FITC (eBioscience, 11-0454-85) and CD45.1-PE-Cy7 (eBioscience, 25-0453-82). For mature cell analyses, unfractionated bone marrow cells were stained with Mac-1-PE-Cy7 (eBioscience, 25-0112-82), Gr-1-PB (eBioscience, 57-5931-82), B220-APC-Cy7 (eBioscience, 47-0452-82), CD19-PE (eBioscience, 12-0193-82), CD4-FITC (BD Biosciences, 553729), and CD8-PE (BioLegend, 100908). For peripheral blood chimaerism analyses, cells were stained with Mac-1-PE-Cy7, Gr-1-PB, B220-APC-Cy7, CD3-APC (eBioscience, 17-0032-82), and Ter-119-PE-Cy5 (eBioscience, 15-5921-83) together with either CD45.2-FITC or CD45.2-Bio followed by SA-Qdot605 and CD45.1-PE (eBioscience, 12-0453). Stained cells were re-suspended in staining media with 1 μg/ml propidium iodide to exclude dead cells. Sorted or gated HSCs were analysed for cell size and NADH autofluorescence using forward scatter (FSC) and UV450/50 channels, respectively. For ROS, mitochondrial mass, and endoplasmic reticulum analyses, sorted HSCs were washed with HBSS, incubated for 15 min at 37 °C with dichlorofluorescin diacetate (DCFDA, 10 μM, Invitrogen, C400), Mitosox Red (MTR, 5 uM, Thermo Fisher Scientific, M36008), Mitotracker Green (MTG, 100 nM, Thermo Fisher Scientific, M7514), or ER-Tracker Green (100 nM, Thermo Fisher Scientific, E34251) in HBSS. For mitochondrial membrane potential or autophagy analyses, sorted HSCs were incubated for 15 min at 37 °C with tetramethylrhodamine-ethyl-ester (TMRE, 200 nM, Enzo, enz-52309) or Cyto-ID (1:1,000, Enzo, ENZ-51031-0050) in staining media. HSCs were then washed with staining media, re-suspended in staining media containing 1 μg/ml propidium iodide, and analysed for dye fluorescence in the FITC or PE channels. For intracellular staining, sorted HSCs were washed in PBS, fixed in Cytofix/Cytoperm buffer (BD Biosciences), washed in PermWash (BD Biosciences), permeabilized with CytoPerm Plus (BD Biosciences) for 10 min at room temperature, re-fixed in Cytofix/Cytoperm buffer for 10 min at 4 °C, washed in PermWash, and incubated in PermWash overnight at 4 °C with the following primary antibodies: rabbit anti-phospho-S6 (Cell Signaling, 2211) or anti-phospho-S6 A488 (Cell Signaling, 4854), and guinea pig anti-p62 (Progen, GP62-C). Cells were then washed in PermWash and incubated in PermWash for 2 h at 4 °C with the appropriate secondary antibody: anti-rabbit A488 (Invitrogen, A21206) or A594 (Invitrogen, A11037), and anti-guinea pig A488 (Invitrogen, A11073) or A647 (Abcam, ab150187). Cells were washed once more in PermWash and re-suspended in PermWash for analyses. For intracellular bromodeoxyuridine (BrdU) staining, Cytofix/Cytoperm-treated HSCs were incubated for 30 min with 0.5 U/μl DNaseI in 3% BSA/0.2× PBS/5 mM $MgCl_2$/2 mM $CaCl_2$ at room temperature, washed in PermWash, incubated with mouse anti-BrdU primary antibody for 30 min at room temperature, washed in PermWash, incubated with APC-conjugated goat anti-mouse (Thermo Fisher Scientific, A21241) secondary antibody for 30 min at room temperature, washed once more in PermWash, and re-suspended for analyses. For intracellular Ki67 and 4′,6-diamidino-2-phenylindole (DAPI, Sigma-Aldrich, 32670-5MG-F) staining, unfractionated bone marrow cells were first stained with Lin/PE-Cy5, c-Kit-APC-eFluor780, Sca-1-PE-Cy7, CD150-PE, and CD48-A647 as described above, and then stained with anti-Ki67 (eBioscience, 11-5698-80) in PermWash for 2 h at 4 °C. Cells were then washed with PermWash, re-suspended in PBS/3% FBS containing 1 μg/ml DAPI, and incubated for 20 min before analysis. Cell isolation was performed on a FACSAria III (Becton Dickinson) using double sorting, and cell analyses were performed using a FACSAria or FACS LSR II using DIVA software (Becton Dickinson).

Cell culture. All cultures were performed at 37 °C in a 5% CO_2 water jacket incubator (Thermo Fisher Scientific). Cells were grown in StemPro34 medium (Invitrogen) supplemented with penicillin (50 U/ml)/streptomycin (50 μg/ml) and L-glutamine (2 mM), with or without the following cytokines (±cyt): SCF (25 ng/ml), Flt3L (25 ng/ml), IL-11 (25 ng/ml), IL-3 (10 ng/ml), GM-CSF (10 ng/ml), Epo (4 U/ml), and Tpo (25 ng/ml) (Peprotech). For self-renewal cultures, only SCF, IL11, and Flt3L were used. BafA (5 nM, Sigma, B1793-2UG), rapamycin (200 nM, EMD Millipore, CAS 53123-88-9), Ink128 (200 nM, a gift from D. Ruggero), AICAR (5 mM, Sigma, A9978), Compound C (CC, 40 μM, EMD Millipore, 171260), or corresponding vehicles (that is, DMSO or water) were added to the ±cyt media when indicated. For glutamine starvation experiments, L-glutamine was omitted from the +cyt medium. For apoptosis and ATP assays, HSCs (400 cells per well) were sorted directly into 40 μl of staining media in 384-well solid white luminescence plates and 40 μl of either Caspase-Glo 3/7 (Promega, G8091) or CellTiter-Glo (Promega, G7570) was then directly added to each well. Both assays were performed according to the manufacturer's instructions and read on a luminometer (Synergy2, BioTek). For colony-forming unit assays, unfractionated bone marrow cells (10,000 cells per 1 ml in a 3-cm dish) or sorted HSCs (100 cells per 1 ml in a 3-cm dish, or 1 cell in 100 μl per well of a 96-well plate) were cultured in methylcellulose (Stem Cell Technologies, M3231) supplemented with L-glutamine, penicillin/streptomycin and the cytokines described above, together with BafA when indicated. Three 3-cm dishes or 60–72 individual cells in 96-well plates were scored per condition after 8–12 days of culture. For measurement of glucose uptake, HSCs (400–2,000 cells) were grown in +cyt media containing 100 μM 2-(*n*-(7-nitrobenz-2-oxa-1,3-diazol-4-yl)amino)-2-deoxyglucose (2-NBD glucose, Invitrogen, N13195). Cells were then washed once in staining media, re-suspended in staining media containing 1 μg/ml propidium iodide, and analysed

© 2017 Macmillan Publishers Limited, part of Springer Nature. All rights reserved.

for 2-NBD glucose fluorescence in the FITC channel. For measurement of glucose uptake in GFP–LC3 HSCs, 6,000 HSCs were cultured with 100 μM 2-deoxyglucose (2-DG) for 4 h and then processed according to the manufacturer's instructions (Glucose Uptake-Glo Assay, Promega, J1341). For BrdU incorporation assays, HSCs (1,000–2,000 cells) were directly sorted into 96-well plates, cultured for 3 h with 60 μM BrdU (Sigma, B5002), and analysed by flow cytometry as described above. For measurement of nascent protein synthesis, HSCs were cultured with 20 μM *O*-propargyl-puromycin (OP-puro, Thermo Fisher Scientific, C10457) for 30 min in +cyt media, processed according to the manufacturer's instructions, and analysed by immunofluorescence staining as described below. For replication stress assays, cells were cultured with the same cocktail of cytokines and aphidicolin (50 ng/ml, Sigma, A4487) in Iscove's modified Dulbecco's media (IMDM) supplemented with 5% FBS (StemCell Technology, 06200), 1× penicillin/streptomycin, 0.1 mM non-essential amino acids, 1 mM sodium pyruvate, 2 mM L-glutamine, and 50 μM 2-mercaptoethanol.

Immunofluorescence staining. HSCs (400–1,500 cells) were sorted directly onto poly-lysine coated slides (VWR International, P-4981) and fixed in PBS/4% PFA for 10 min at room temperature. Slides were permeabilized in PBS/0.15% Triton X-100 for 2 min at room temperature and blocked in PBS/1% BSA for 1 h at room temperature. Slides were then incubated in PBS/1% BSA with either rabbit anti-FoxO3a (Millipore, 07-1719), mouse anti-phospho-H2AX (Ser139) (Millipore, 05-636), rabbit anti-53BP1 (Novus Biologicals, NB100-904), rabbit anti-FBL (Cell Signaling, 2639), mouse anti-RAD51 (Abcam, ab1837), mouse anti-LAMP1 (Developmental Studies Hybridoma Bank, 1D4B), mouse anti-KDEL (Abcam, ab12223), or rabbit anti-TOM20 (Santa Cruz Biotechnology, sc-11415) for 1 h at 37 °C. Slides were then washed three times in PBS and incubated for 1 h at 37 °C in PBS/1% BSA with appropriate secondary antibodies (all from Life Technologies): A488-conjugated goat anti-mouse (A-11029), A594-conjugated goat anti-rabbit (A-11037), A594- or A488-conjugated goat anti-rat (A-11007, A-10528), and A488-conjugated donkey anti-mouse (A-21202). Slides were finally washed three times in PBS and mounted using VectaShield (Vector Laboratories) containing 1 μg/ml DAPI. EdU incorporation was detected using A594-labelled azide click chemistry according to the manufacturer's instructions (Life Technologies, Click-iT EdU imaging assay, C10339). For OP-puro analysis, after processing, slides were stained with anti-phospho-H2AX and then A488-conjugated goat anti-mouse. Cells were imaged on a SP5 Leica Upright Confocal Microscope (20× or 63× objective), and images were processed using Volocity software (version 4.4, Improvision, Waltham, Massachusetts, USA) and ImageJ. Between five and eight *z*-stacks were taken per image, and total fluorescence per cell was measured using Volocity on ≥20 cells per condition.

***In vitro* assays.** For western blot analyses, sorted HSCs (~30,000 cells per condition) were lysed in RIPA buffer, run on standard 12% SDS–PAGE gels, transferred onto nitrocellulose membranes (Bio-Rad, 162-0232), and blocked with 5% bovine serum albumin (BSA) in blocking buffer (Li-COR Biosciences, 927-40000) containing 0.1% Tween (BBT) for 1 h at room temperature according to standard protocols. Membranes were incubated for overnight at 4 °C in BBT with primary antibodies in BBT, washed once with BBT, incubated for 1 h at 4 °C in BBT with appropriate secondary antibodies, and detected on an Odyssey Infrared Imaging System (Li-COR Biosciences). Membranes were eventually stripped with NewBlot Stripping Buffer Nitro (Li-COR Biosciences, 928-40030) according to the manufacturer's instructions before being re-incubated with another primary antibody. Rabbit anti-phospho-AMPKα (Cell Signalling, 2535), rabbit anti-phospho-S6 (Cell Signalling, 2215), mouse anti-S6 (Cell Signalling, 2317), and rabbit anti-actin (Sigma-Aldrich, A2066) were used as primary antibodies and IRDye 800CW Goat Anti-Rabbit IgG (Li-COR Biosciences, 926-32211) or IRDye 800CW Goat Anti-Mouse IgG (Li-COR Biosciences, 926-32210) as secondary antibodies. For Seahorse metabolic flux experiments, oxygen consumption rates and extracellular acidification rates were measured using a 96-well Seahorse Bioanalyzer XF 96 according to the manufacturer's instructions (Agilent Technologies). In brief, HSCs or LSK cells (75,000 cells per well) were sorted directly into 96-well plates pre-coated for 3 h with poly-lysine (Sigma-Aldrich, P4707) and containing cyt+ media. Plates were then centrifuged for 5 min at 1,200 r.p.m. and media was replaced with 175 μl of temperature/CO_2 pre-adjusted +cyt media. Plates were either immediately analysed or cultured for 22 h before analysis according to the manufacturer's instructions with the following exceptions. For glycolysis assays, the starting +cyt media already contained glucose and 2 μM oligoymycin followed by 1 M 2-DG was used. For OXPHOS assays, 1 μM oligomycin followed by 2 μM FCCP was used. For both assays, mix and read times were also extended to 7 min and 4 min, respectively. For electron microscopy analyses, cells (40,000–75,000 per condition) were pelleted for 5 min at 4 °C at 600*g*, fixed on ice for 30 min in 0.1 M NaCacodylate, pH 7.4, containing 2% glutaraldehyde and 1% PFA, and pelleted at 3,000*g* for 10 min at 4 °C. Samples were then submitted to the Gladstone Institutes (UCSF) Electron Microscopy Core Facility for standard transmission electron microscopy ultrastructural analyses. Mitochondria numbers and morphology were visually scored. For αKG measurements, 10^6 c-Kit-enriched bone marrow cells were processed according to the manufacturer's instructions (Biovision, K677-100). For SAM measurements, 15,000 HSCs were processed according to the manufacturer's instructions (Mediomics, 1-1-1004).

Gene expression analyses. For microarray analyses, RNA was purified from sorted HSCs and GMPs (7,000–20,000 cells obtained from individual mice) using an Arcturus PicoPure RNA Isolation Kit, amplified using an Ovation Pico WTA System V2 (NuGEN, 3302-12), fragmented and biotinylated using the Encore Biotin Module (NuGEN, 4200-12), and hybridized on Affymetrix Gene ST 1.0 microarrays according to the manufacturers' instructions. Transcriptome profiling was performed at the Gladstone Institutes Genomics Core (UCSF). Gene expression was first measured at the probe set level ($n = 241{,}619$) using robust multi-array average methodology followed by quantile normalization[37]. Quality of the data was assessed using principal component analysis as well as unsupervised hierarchical clustering. Probe set annotation for the MoGene1.0st version 1 array was downloaded from Affymetrix's website and the 241,619 probe sets were mapped to the 28,853 main transcript set (excluding controls). This data set was used for all analyses. We used a family of generalized, linear models implemented with the R package, LIMMA, to assess differential expression between groups of interest[38]. Nominal *P* values were corrected for multiple comparisons using a false discovery rate cutoff of 0.05. Gene set enrichment analyses were performed according to standard procedures on curated gene sets from previous publications. Normalized expression values for each replicate were used to generate an expression data set file, and gene set enrichment analyses was run using the weighted enrichment score. DAVID was used to functionally annotate the differentially expressed or methylated genes to Gene Ontology terms. For Fluidigm analyses, the Fluidigm 96.96 Dynamic Array integrated fluidic circuit was used and analyses were performed as previously described[36]. Briefly, HSCs or MPPs (100 cells per well) were directly sorted into 96-well plates containing CellsDirect lysis buffer (Invitrogen, 11753-100), reverse-transcribed and pre-amplified for 18 cycles using Superscript III Platinum Taq DNA polymerase (Invitrogen, 18080-044) with a custom-made set of 96 proprietary target-specific primers (Fluidigm). The resulting cDNAs were analysed on a Biomark system (Fluidigm) using EvaGreen Sybr dye (Bio-Rad, 172-5211). Data were collected with Biomark Data Collection Software (Fluidigm) and analysed using Biomark qPCR analysis software with a quality threshold of 0.65 and linear baseline correction. Melt curves and melting temperature (T_m) values for each assay reaction were checked individually, and reactions with melt curves showing multiple peaks or poor quality were discarded, leaving 69 genes for further analyses. For gene expression quantification, data were exported as a Microsoft Excel .csv file and analysed by the $\Delta\Delta C_t$ method using *Actb* normalization.

Methylation analyses. DNA was isolated from sorted HSCs (4,000–24,000 cells obtained from individual mice) using an Allprep DNA/RNA Mini Kit (Qiagen, 80204) and used for library preparation. Enhanced reduced-representation bisulfite sequencing was performed as previously described[39], except for gel size selection as only fragments of 150–450 bp were excised owing to the low input amount of starting DNA. Libraries were sequenced on an Illumina HiSeq 2500. Reads were aligned against a bisulfite-converted mouse genome (mm10) using Bowtie and Bismark (versions 2.2.6 and 0.14.5, respectively). After filtering and normalizing by coverage, differentially methylated cytosines were identified using MethylKit (version 0.9.4) and R statistical software (version 3.2.1)[40]. Significant DMRs were identified with eDMR (version 0.6.3.1) using the following parameters: ≥2 differentially methylated cytosines, ≥3 CpG, mean methylation difference ≥ 20, and DMR *q* value ≥ 0.05. DMRs were annotated to the RefSeq genes as previously described[41]. DAVID was used to functionally annotate the differentially methylated genes to Gene Ontology terms, SP_PIR_KEYWORDS, and KEGG Pathways with a false discovery rate cutoff of 0.1. ChIP-enrich was used to functionally annotate the differentially methylated genes to Gene Ontology terms and KEGG Pathways with a false discovery rate cutoff of 0.05. Maximum gene set size was limited to 500, and DMR were annotated to the nearest gene.

Statistics. All experiments were repeated as indicated; *n* is the number of independent biological repeats. Numbers of independent experiments are reported in the Supplementary Information. Data are expressed as mean ± standard deviation (s.d.), or standard error of the mean (s.e.m.) as indicated when a group within an experiment had fewer than three independent repeats, and for all line graph visualization of results. Mice for transplantation were randomized, samples were alternated whenever possible, and no blinding protocol was used. No statistical method was used to predetermine sample size. *P* values were generated using two-tailed Student's *t*-test, and were considered significant when ≤0.05. All experiments were repeated as indicated; *n* is the number of independent biological repeats that

© 2017 Macmillan Publishers Limited, part of Springer Nature. All rights reserved.

are distinct individual or pooled mice, except when indicated otherwise in the figure legends. Pooled mice were used for Figs 2a, f–j, 3a, d, e, 4a, g, 5d and 6b, and Extended Data Figs 1k, 3b, 4d, f, g, i, 5a, e, 6a–d, 7c, g and 9b, c.

Data availability. Data sets that support the findings of this study have been deposited in the Gene Expression Omnibus under accession number GSE81721. Source Data for all the figures are provided with the paper. All other data are available from the corresponding author upon reasonable request.

34. Kühn, R., Schwenk, F., Aguet, M. & Rajewsky, K. Inducible gene targeting in mice. *Science* **269,** 1427–1429 (1995).
35. Hara, T. *et al.* Suppression of basal autophagy in neural cells causes neurodegenerative disease in mice. *Nature* **441,** 885–889 (2006).
36. Pietras, E. M. *et al.* Functionally distinct subsets of lineage-biased multipotent progenitors control blood production in normal and regenerative conditions. *Cell Stem Cell* **17,** 35–46 (2015).
37. Bolstad, B. M., Irizarry, R. A., Astrand, M. & Speed, T. P. A comparison of normalization methods for high density oligonucleotide array data based on variance and bias. *Bioinformatics* **19,** 185–193 (2003).
38. Ritchie, M. E. *et al.* limma powers differential expression analyses for RNA-sequencing and microarray studies. *Nucleic Acids Res.* **43,** e47 (2015).
39. Akalin, A. *et al.* Base-pair resolution DNA methylation sequencing reveals profoundly divergent epigenetic landscapes in acute myeloid leukemia. *PLoS Genet.* **8,** e1002781 (2012).
40. Akalin, A. *et al.* methylKit: a comprehensive R package for the analysis of genome-wide DNA methylation profiles. *Genome Biol.* **13,** R87 (2012).
41. Meldi, K. *et al.* Specific molecular signatures predict decitabine response in chronic myelomonocytic leukemia. *J. Clin. Invest.* **125,** 1857–1872 (2015).

© 2017 Macmillan Publishers Limited, part of Springer Nature. All rights reserved.

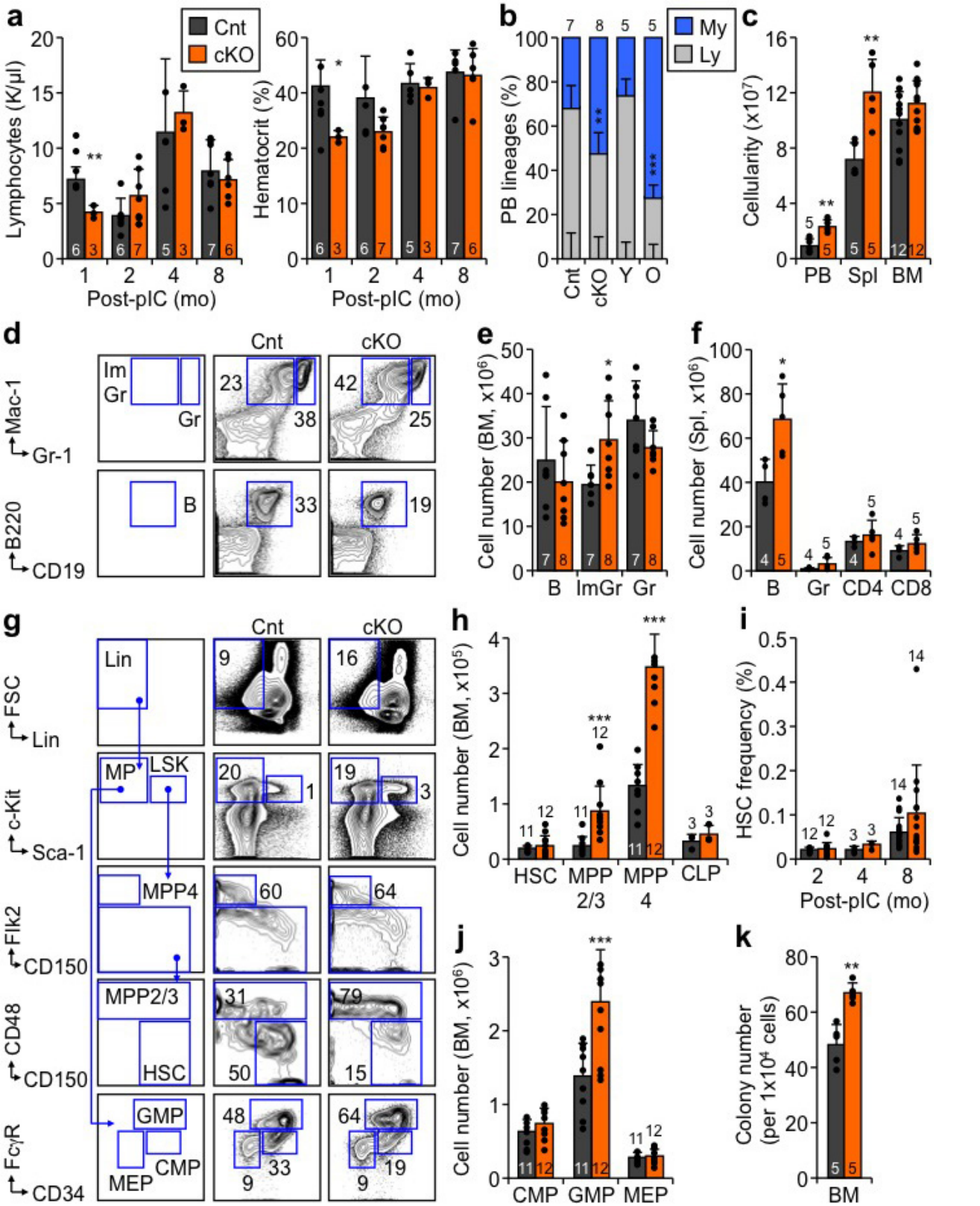

Extended Data Figure 1 | Characterization of autophagy-deficient *Atg12*^{cKO} mice. a, Complete blood count analyses of lymphocytes and haematocrit in control (Cnt) and *Atg12*^{cKO} (cKO) mice after pIC treatment. **b**, Lineage distribution in peripheral blood of control and cKO mice at 2 months after pIC, and in young and old mice. My, myeloid; Ly, lymphoid. **c**, Total cell numbers in peripheral blood, spleen (Spl), and bone marrow of control and cKO mice at 2 months after pIC. **d**, Gating strategy for mature populations. ImGr, imature granulocytes/monocytes; Gr, granulocyte; B, B cells. **e**, **f**, Mature populations in (**e**) bone marrow and (**f**) spleen of control and cKO mice at 2 months after pIC. **g**, Gating strategy for immature bone marrow populations. Lin, lineage negative; MP, myeloid progenitors; CMP, common myeloid progenitor; MEP, megakaryocyte/erythrocyte progenitor. **h**, Quantification of immature bone marrow populations in control and cKO mice at 2 months after pIC. CLP, common lymphoid progenitor. **i**, HSC frequency over time in control and cKO mice after pIC. **j**, Quantification of MP bone marrow populations in control and cKO mice at 2 months after pIC. **k**, Colony formation in methylcellulose from control and cKO bone marrow at 2 months after pIC. Data are mean ± s.d. $^{*}P \leq 0.05$, $^{**}P \leq 0.01$, $^{***}P \leq 0.001$.

© 2017 Macmillan Publishers Limited, part of Springer Nature. All rights reserved.

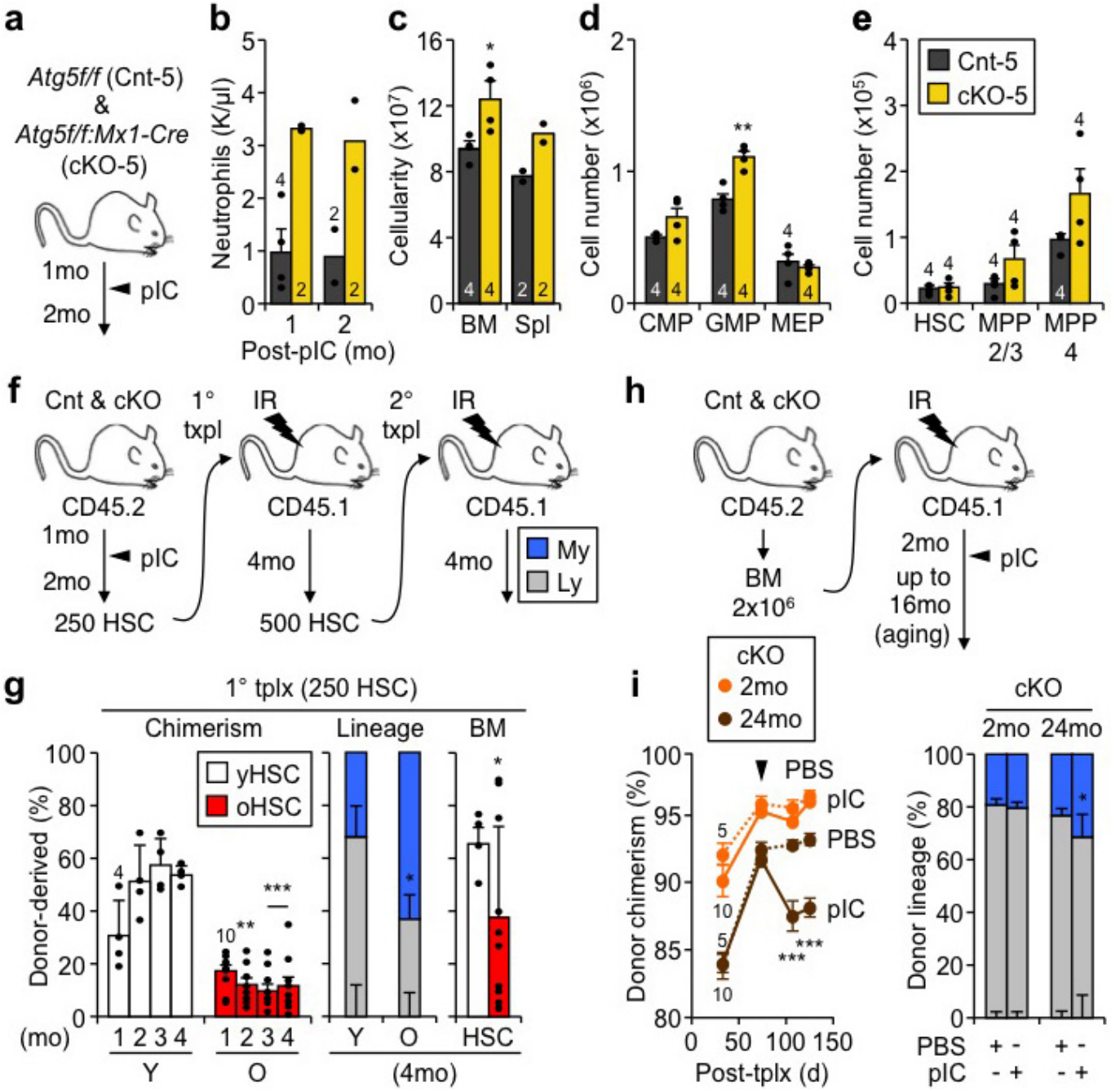

Extended Data Figure 2 | Characterization of autophagy-deficient *Atg12*^{cKO} mice and regenerative capacity of *Atg12*^{cKO} HSCs. **a**–**e**, Haematopoietic features of control (Cnt-5) and *Atg5*^{cKO} (cKO-5) mice after pIC treatment: (**a**) scheme for deleting A*tg5* in the adult blood system, and (**b**) neutrophil counts in peripheral blood, (**c**) total cell numbers in bone marrow and spleen, and quantification of (**d**) MP and (**e**) immature bone marrow populations at 2 months after pIC. **f**, Scheme for control and cKO HSC primary (1°) and secondary (2°) transplantation (tplx). **g**, Engraftment of young (Y) and old (O) HSCs with donor chimaerism in peripheral blood over time (left), and lineage distribution in peripheral blood (centre) with HSC chimaerism (right) at the indicated time after transplantation. **h**, Scheme for ageing recipients transplanted with non-pIC-treated control and cKO bone marrow cells and subsequently deleted for *Atg12*. **i**, *Atg12* deletion in recipients transplanted with 2×10^6 bone marrow cells from 2- or 24-month-old non-pIC-treated cKO donors with donor chimaerism in peripheral blood after PBS or pIC (left, ± s.e.m.), and lineage distribution in peripheral blood at 125 d after transplantation (right). Data are mean ± s.d. except where indicated. $^*P \leq 0.05$, $^{**}P \leq 0.01$, $^{***}P \leq 0.001$.

© 2017 Macmillan Publishers Limited, part of Springer Nature. All rights reserved.

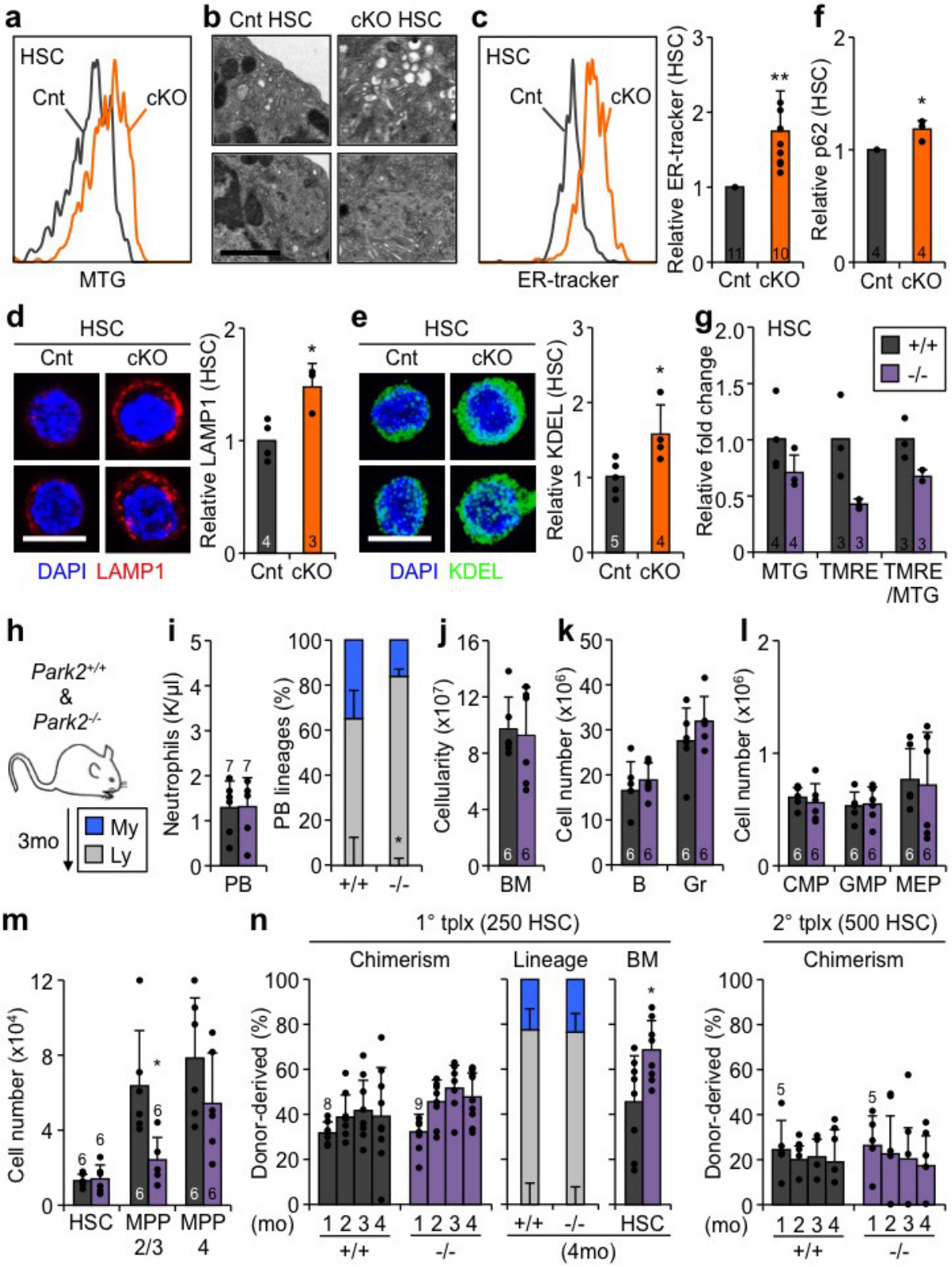

Extended Data Figure 3 | Altered biology of *Atg12*^{cKO} HSCs and characterization of *Park2*$^{-/-}$ mice. a, Representative FACS plot of MTG staining in control and cKO HSCs. **b**, Representative electron micrographs depicting expanded small vesicles (top) and endoplasmic reticulum/Golgi (bottom) in control and cKO HSCs. Scale bar, 1 μm. **c**, Representative FACS plot and quantification of endoplasmic reticulum mass measured by ER-Tracker flow cytometry staining in control and cKO HSCs. **d**, **e**, Representative immunofluorescence images and quantification of (**d**) LAMP1 and (**e**) KDEL staining in control and cKO HSCs. Scale bars, 10 μm. **f**, Levels of p62 in control and cKO HSCs. **g**, Mitochondria parameters in *Park2*$^{+/+}$ and *Park2*$^{-/-}$ HSCs. **h**–**m**, Characterization of *Park2*$^{-/-}$ mice: (**h**) scheme for analyses, (**i**) complete blood count parameters (left) and lineage distribution in peripheral blood (right), (**j**) bone marrow total cell numbers, (**k**) bone marrow mature populations, and (**l**, **m**) bone marrow immature populations. **n**, Transplantation of *Park2*$^{-/-}$ HSCs showing donor chimaerism (left) and lineage distribution (centre) in peripheral blood, and HSC chimaerism (right) at the indicated time after transplantation in primary and secondary recipients. Data are mean ± s.d. $^{*}P \leq 0.05$, $^{**}P \leq 0.01$, $^{***}P \leq 0.001$.

© 2017 Macmillan Publishers Limited, part of Springer Nature. All rights reserved.

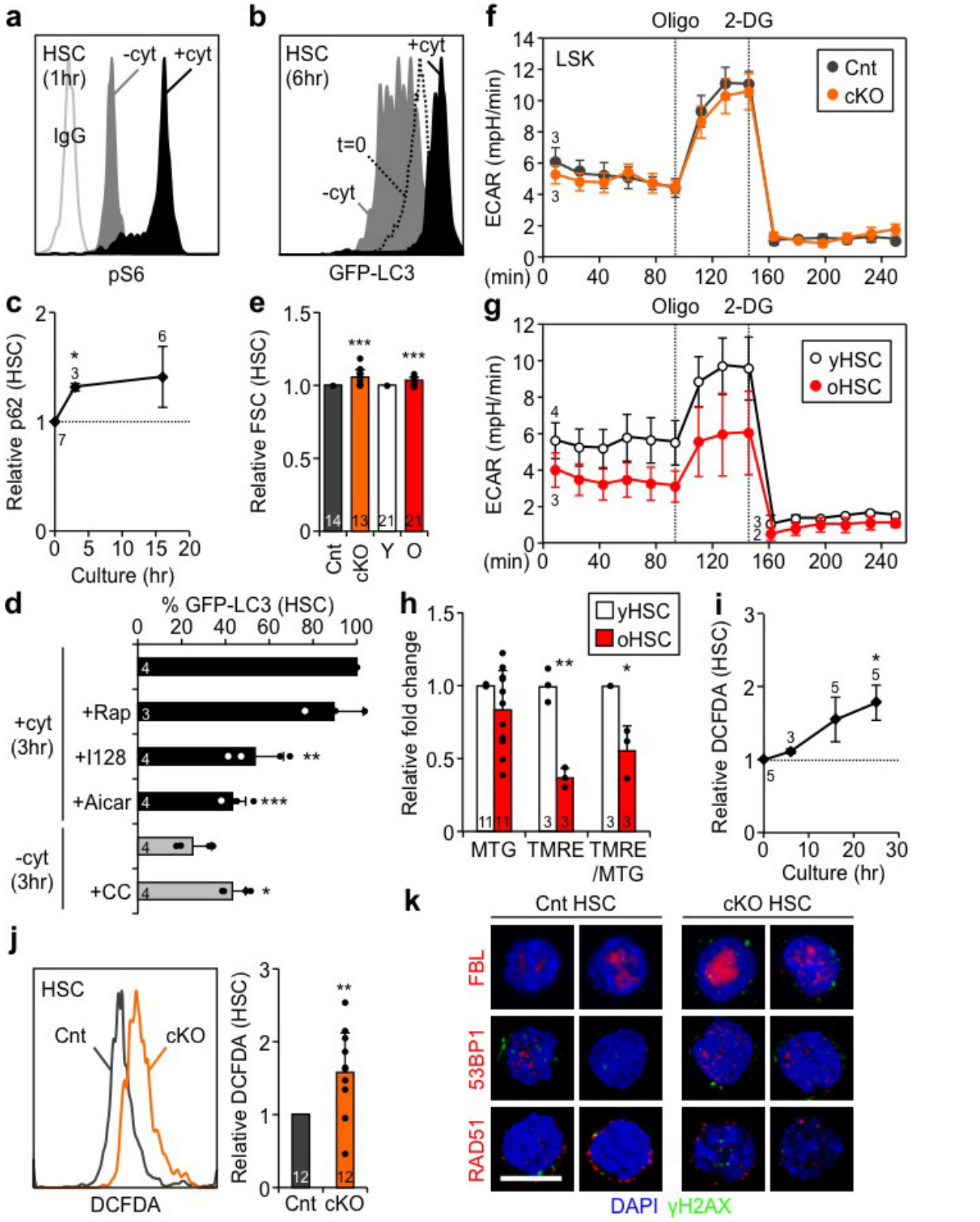

Extended Data Figure 4 | Comparison between aHSCs, *Atg12*^{cKO} HSCs and oHSCs. a, Representative FACS plot of pS6 levels in HSC cultured for 1 h (hr) with or without cytokines (±cyt). **b**, Representative FACS plot of GFP–LC3 in freshly isolated HSCs ($t = 0$) and HSCs cultured for 6 h with or without cytokines. **c**, Inactivation of autophagy in +cyt measured by p62 levels. **d**, Drug modulation of autophagy levels in *Gfp–Lc3* HSCs cultured for 3 h with or without cytokines. Rap, rapamycin; I128, Ink128; CC, compound C. Results are expressed as percentage GFP–LC3 levels upon 3 h culture in +cyt conditions. **e**, Cell size measured by forward scatter (FSC) in control and cKO HSCs, and yHSCs and oHSCs. **f**, **g**, Glycolysis activity measured by extracellular acidification rate (ECAR) in (**f**) control and cKO LSKs, and (**g**) yHSCs and oHSCs. Oligo, oligomycin; 2-DG, 2-deoxy-D-glucose. **h**, Mitochondria parameters in yHSCs and oHSCs. **i**, ROS levels in aHSCs. **j**, Representative FACS plot and quantification of ROS levels in control and cKO HSCs. **k**, Representative examples of three independent experiments showing immunofluorescence co-staining of γH2AX with fibrillarin (FBN), 53BP1, and RAD51 in control and cKO HSCs. Sscale bar, 10 μm. Data are mean ± s.d. except for line graphs, and are expressed relative to 0 h HSC (**c**, **i**), control HSC (**e**, **j**), or yHSC (**e**, **h**) levels. *$P \leq 0.05$, **$P \leq 0.01$, ***$P \leq 0.001$.

© 2017 Macmillan Publishers Limited, part of Springer Nature. All rights reserved.

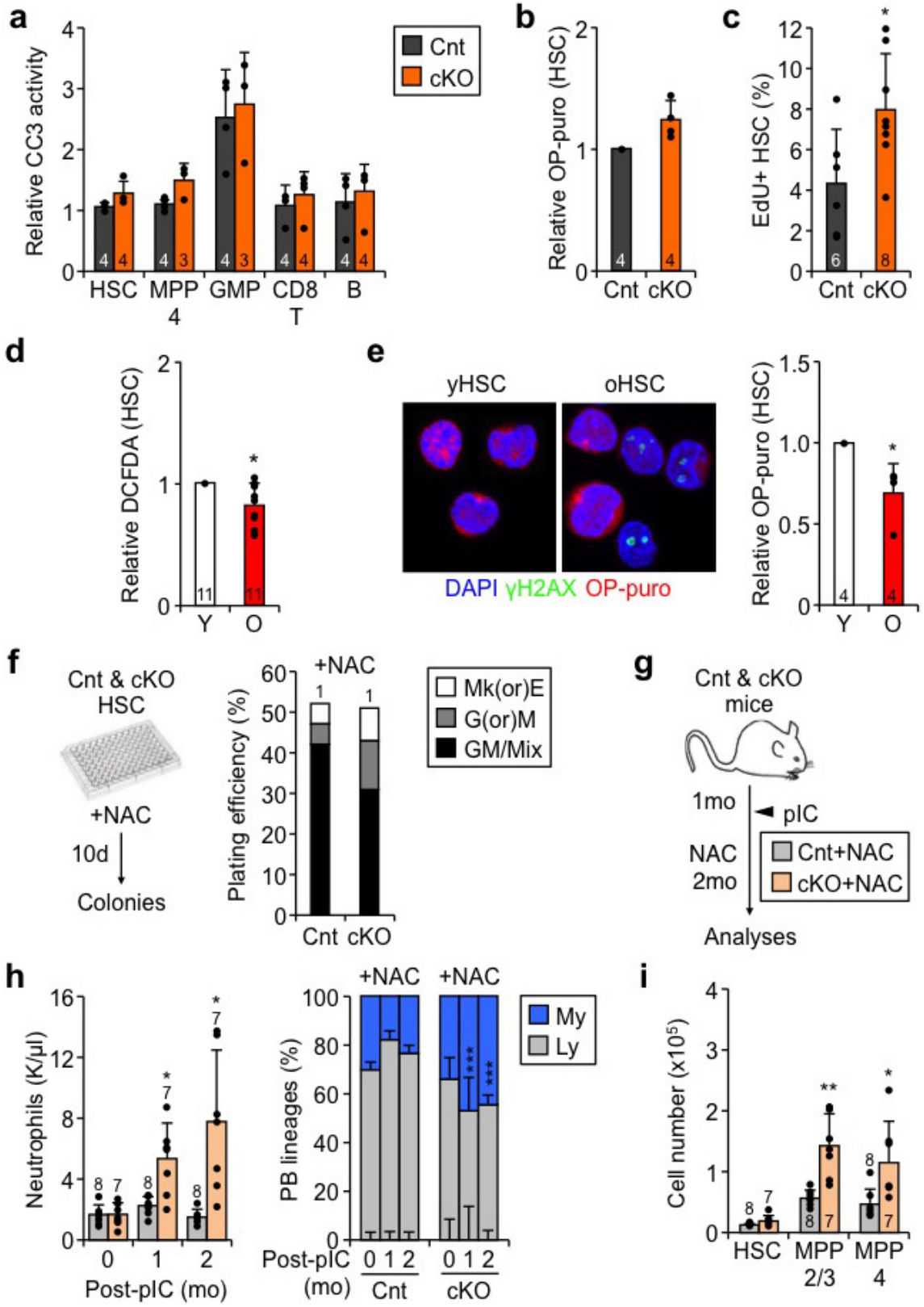

Extended Data Figure 5 | Properties of autophagy-deficient and oHSCs, and effect of ROS scavenging in *Atg12*^{cKO} mice. **a**–**c**, Characteristics of control and cKO HSCs: (**a**) apoptosis measured by cleaved caspase 3 (CC3) activity, (**b**) protein synthesis measured by *O*-propargyl-puromycin (OP-puro) immunofluorescence staining, and (**c**) cycling activity measured by EdU incorporation. **d**, **e**, Characteristics of yHSCs and oHSCs: (**d**) ROS levels and (**e**) protein synthesis with representative OP-puro immunofluorescence staining (left) and quantification (right). **f**, Scheme for NAC *in vitro* treatment and representative example of colony formation in methylcellulose from NAC-treated control and cKO HSCs. CFU, colony-forming unit; Mk(or)E and G(or)M, mature megakaryocyte, erythroid, granulocyte, or macrophage colonies; GM/Mix, immature GM or GMMkE colonies. Results are expressed as percentage of plated cells. **g**–**i**, Scavenging ROS levels in *Atg12*^{cKO} mice: (**g**) scheme for NAC *in vivo* treatment after pIC deletion of *Atg12*, (**h**) neutrophil counts (left) and lineage distribution (right) in peripheral blood, and (**i**) quantification of immature bone marrow populations. Data are mean ± s.d., and are expressed relative to control HSC (**a**, **b**), or yHSC (**d**, **e**) levels. $*P \leq 0.05$, $**P \leq 0.01$.

© 2017 Macmillan Publishers Limited, part of Springer Nature. All rights reserved.

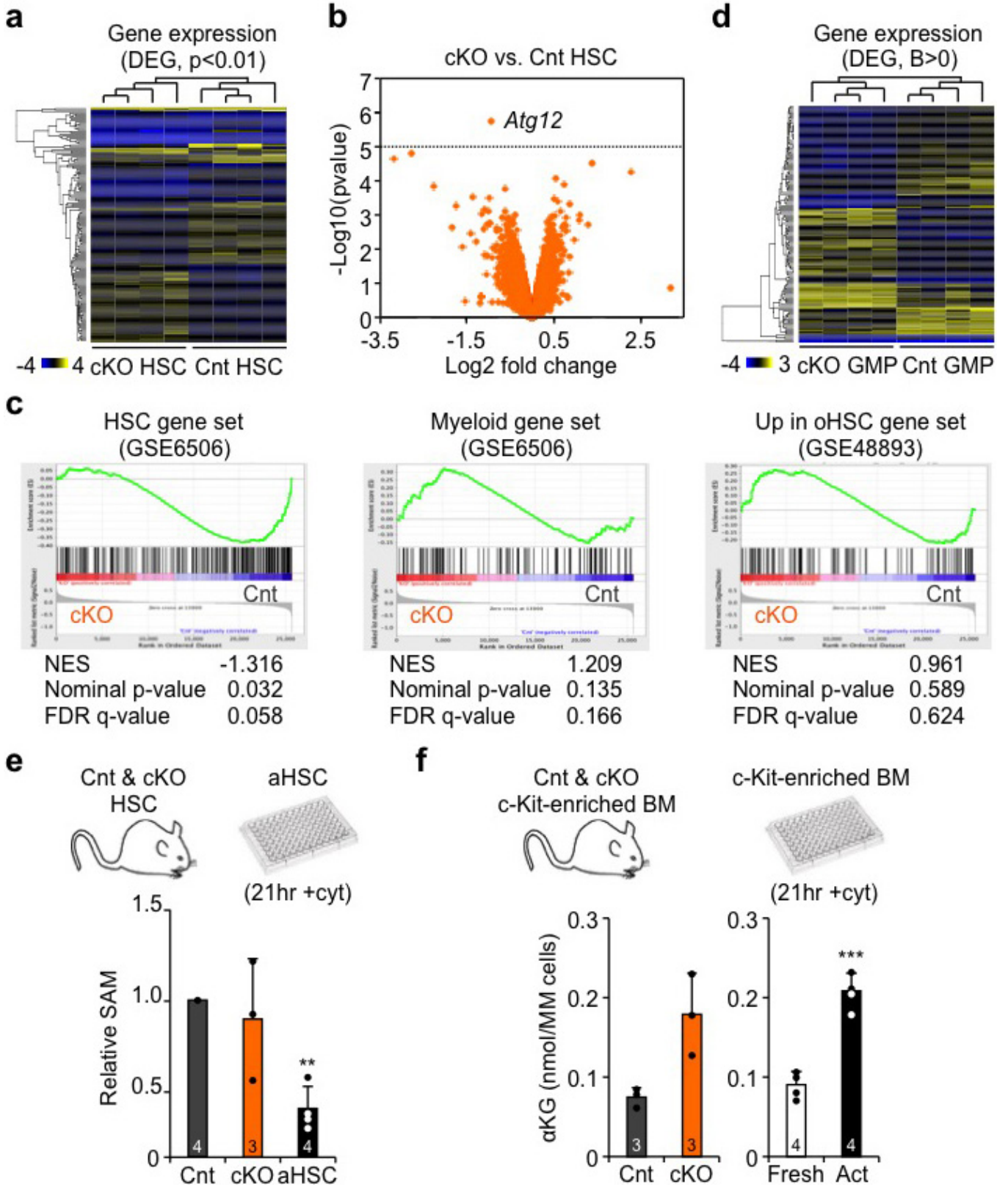

Extended Data Figure 6 | Differential gene expression in *Atg12*^{cKO} HSCs and GMPs, and regulation of DNA methylation in HSCs. **a**, Heatmap of differentially expressed genes (DEG) in cKO versus control HSC microarrays ($n = 4$). **b**, Volcano plot of DEGs in cKO versus control HSCs. **c**, Gene set enrichment analyses (GSEA) of DEGs in cKO versus control HSCs: NES: normalized enrichment score. **d**, Heatmap of DEGs in cKO versus control GMP microarrays ($n = 4$). **e**, SAM levels in control and cKO HSCs, and aHSCs. **f**, αKG levels in c-Kit-enriched control and cKO bone marrow (left, $P = 0.0672$), and freshly isolated and activated c-Kit-enriched bone marrow (right). Data are mean ± s.d. $^{*}P \leq 0.05$, $^{***}P \leq 0.001$.

© 2017 Macmillan Publishers Limited, part of Springer Nature. All rights reserved.

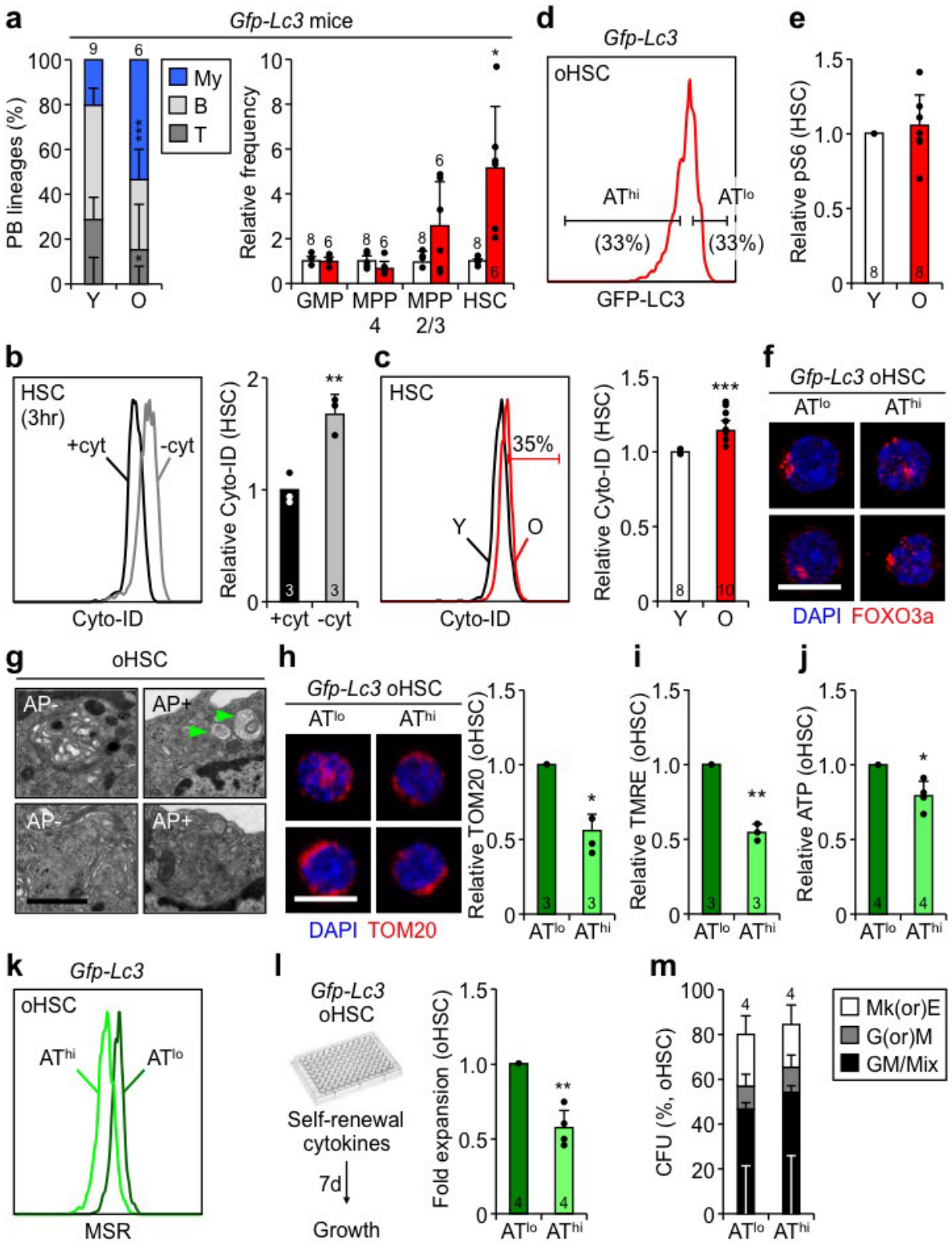

Extended Data Figure 7 | Additional analyses of old *Gfp–Lc3* HSCs. **a**, Lineage distribution in peripheral blood (left) and frequency of the indicated populations (right) in young and old *Gfp–Lc3* mice (related to Fig. 5a, b). **b**, pS6 levels in yHSCs and oHSCs. **c**, **d**, Representative FACS plots and quantification of Cyto-ID dye levels in (**c**) HSCs cultured for 3 h with or without cytokines, and (**d**) yHSCs and oHSCs. **e**, Representative FACS plots of autophagy low (AT^{lo}) and autophagy high (AT^{hi}) oHSC subsets. **f**, Representative examples of three independent experiments showing immunofluorescence staining of FOXO3a in AT^{lo} and AT^{hi} oHSCs. Scale bar, 10 μm. **g**, Representative electron micrographs of oHSCs with or without autophagosomes (AP) showing vesicles (top) and endoplasmic reticulum/Golgi (bottom) compartments. Scale bar, 1 μm. **h**, Representative immunofluorescence staining and quantification of TOM20 in AT^{lo} and AT^{hi} oHSCs. Scale bar, 10 μm. **i**, **j**, Characteristics of AT^{lo} and AT^{hi} oHSCs: (**i**) TMRE levels, (**j**) ATP levels, and (**k**) ROS levels measured by Mitosox Red (MSR) staining. **l**, Expansion of AT^{lo} and AT^{hi} oHSCs in self-renewal culture conditions. **m**, Colony formation in methylcellulose from AT^{lo} and AT^{hi} oHSCs. Results are expressed as percentage of 100 plated cells. Data are mean ± s.d., and are expressed relative to +cyt HSC (**c**), yHSC (**b**, **d**), or AT^{lo} oHSC (**h**–**j**, **l**) levels. $^{*}P \leq 0.05$, $^{**}P \leq 0.01$, $^{***}P \leq 0.001$.

© 2017 Macmillan Publishers Limited, part of Springer Nature. All rights reserved.

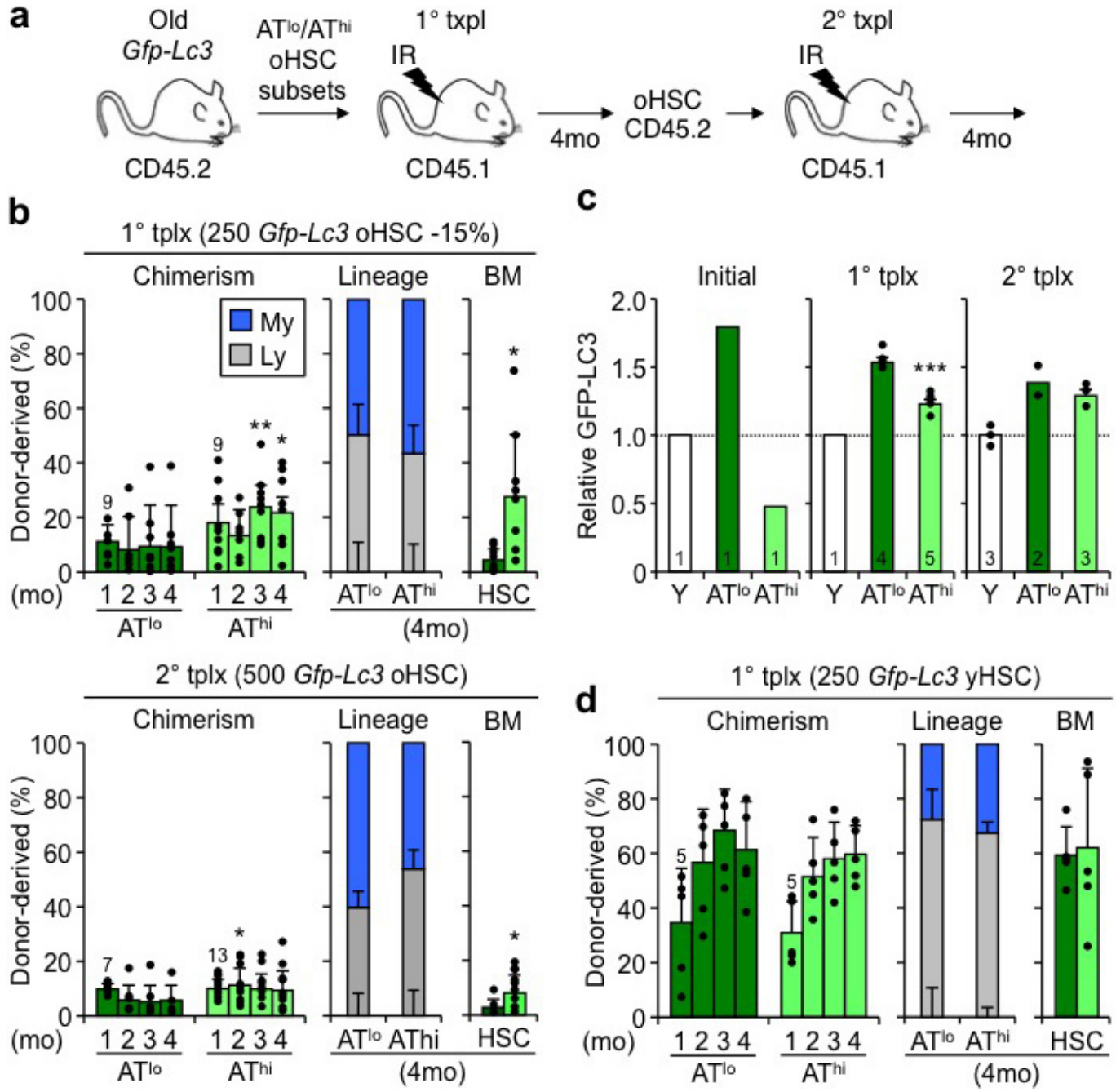

Extended Data Figure 8 | Functionality of AT^{lo} and AT^{hi} oHSC subsets. a, Scheme for primary and secondary transplantations of AT^{lo} or AT^{hi} yHSCs and oHSCs. **b**, Transplantation of AT^{lo} and AT^{hi} oHSC subsets with 15% GFP–LC3 high/low expression cutoff showing donor chimaerism (left) and lineage distribution (centre) in peripheral blood, and HSC chimaerism (right) at the indicated times after transplantation in primary (top row) and secondary (bottom row) recipients. **c**, GFP–LC3 levels in AT^{lo} and AT^{hi} oHSCs before transplantation, and in primary and secondary recipients. Results are expressed relative to GFP–LC3 levels in yHSCs (± s.e.m.). **d**, Transplantation of AT^{lo} and AT^{hi} yHSC subsets with 33% GFP–LC3 high/low expression cutoff showing donor chimaerism (left) and lineage distribution (centre) in peripheral blood, and HSC chimaerism (right) at the indicated times after transplantation in primary recipients. Data are mean ± s.d. except when indicated. $^{*}P \leq 0.05$, $^{**}P \leq 0.01$, $^{***}P \leq 0.001$.

© 2017 Macmillan Publishers Limited, part of Springer Nature. All rights reserved.

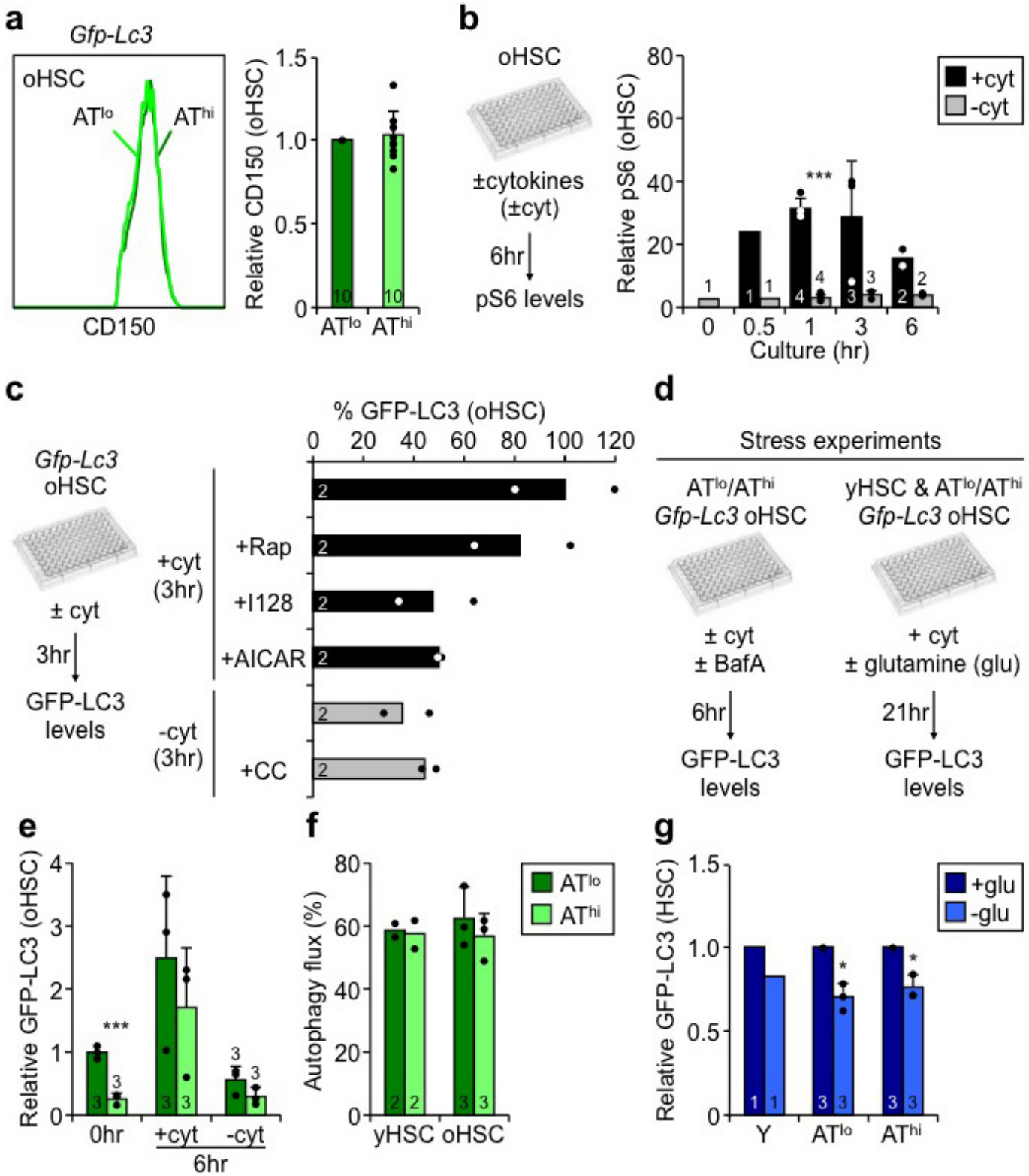

Extended Data Figure 9 | Autophagy capability of AT^{lo} and AT^{hi} oHSC subsets. a, Representative FACS plot and quantification of CD150 levels in AT^{lo} and AT^{hi} oHSCs. **b**, Levels of pS6 measured by flow cytometry in HSCs cultured with or without cytokines for the indicated times. Results are normalized to IgG levels. **c**, Drug modulation of autophagy levels in *Gfp–Lc3* oHSCs cultured for 3 h with or without cytokines. I128, Ink128; CC, compound C. Results are expressed as percentage GFP–LC3 levels upon 3 h culture in +cyt conditions. **d**, Scheme for the stress experiments assessing the autophagy capability of AT^{lo} and AT^{hi} oHSCs. **e**, **f**, Response to cytokine starvation with (**e**) GFP–LC3 levels in freshly isolated ($t = 0$) and upon 6 h culture in ±cyt conditions, and (**f**) autophagy flux after 6 h culture in ±cyt ±BafA conditions. Percentage flux is calculated as $[100 \times (1 - (-\text{BafA}/+\text{BafA}))]$. **g**, Response to glutamine (glu) deprivation. Data are mean ± s.d. and are expressed relative to AT^{lo} oHSC (**a**, **e**) or freshly isolated ($t = 0$) oHSC (**b**) levels, or relative to +glu conditions (**g**). ***$P \leq 0.001$.

© 2017 Macmillan Publishers Limited, part of Springer Nature. All rights reserved.

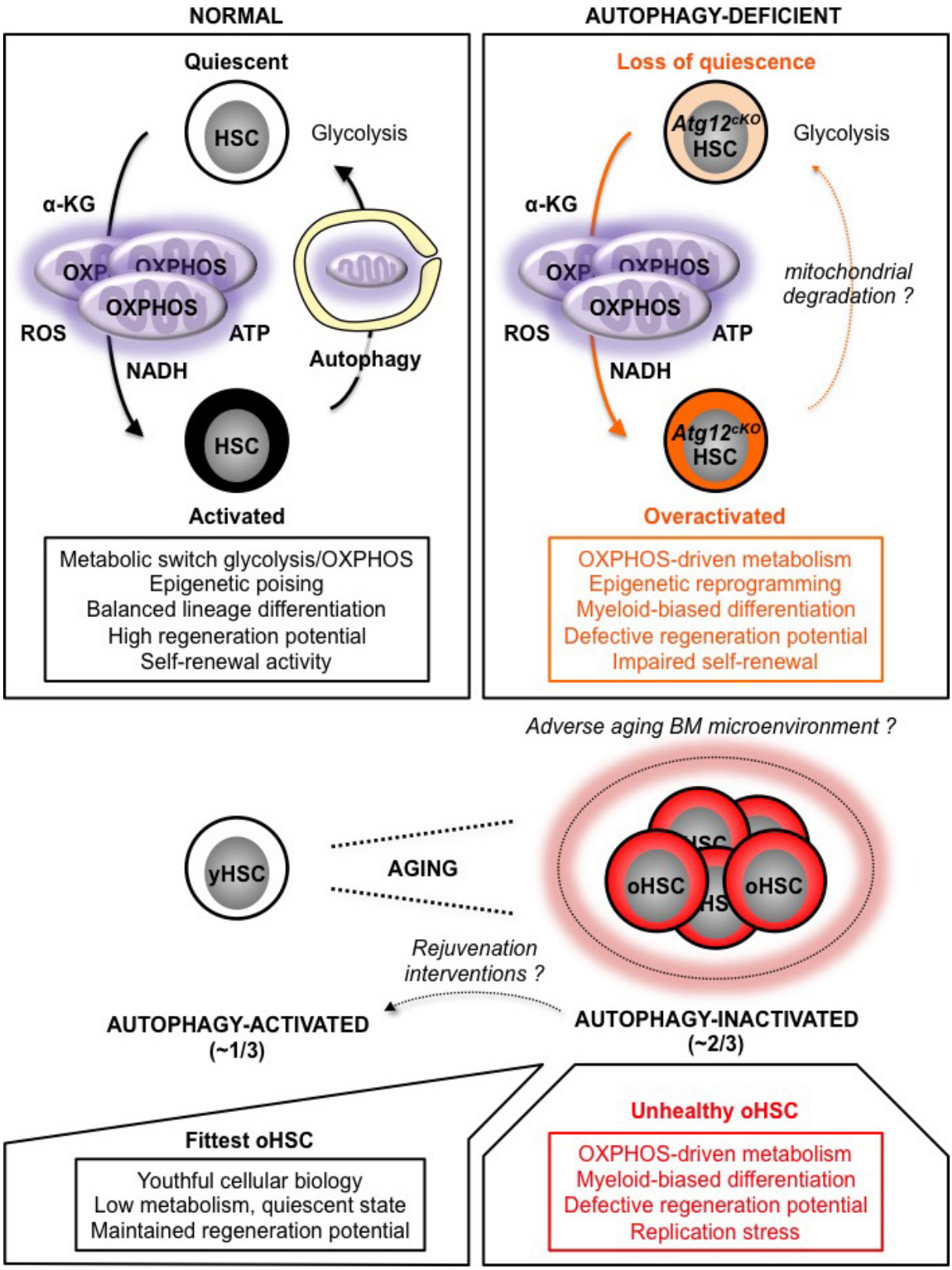

Extended Data Figure 10 | See next page for caption.

© 2017 Macmillan Publishers Limited, part of Springer Nature. All rights reserved.

Extended Data Figure 10 | Model for the role of autophagy in HSC function and HSC ageing. HSC activation is accompanied by mitochondria activation and a shift in metabolic activity from glycolysis to OXPHOS, which provides energy and increases the production of mitochondrial metabolites such as α-ketoglutarate (αKG) that act as substrates/co-factors for epigenetic enzymes. Metabolically, aHSCs are poised to undergo lineage priming and produce differentiated progeny to regenerate the blood system. However, aHSCs must also return to quiescence to maintain the stem cell pool. In this context, autophagy plays an essential role by clearing active mitochondria to allow OXPHOS-driven HSCs to efficiently revert to a mostly glycolysis-based metabolic quiescence. Without autophagy, HSCs display an overactive OXPHOS-driven metabolism that promotes myeloid-biased differentiation and loss of stemness as a consequence of epigenetic reprogramming. Other mechanisms of mitochondria elimination probably allow some autophagy-deficient HSCs to return to quiescence during homeostasis, but they do not substitute for autophagy in maintaining HSC function in conditions of intense regeneration stress such as transplantation. This role of autophagy becomes even more important with age as the inability of about two-thirds of oHSCs to activate autophagy results in an overactive OXPHOS metabolism that impairs self-renewal, promotes proliferation and myeloid differentiation, and contributes to replication stress. These unhealthy oHSCs drive most of the ageing blood phenotypes. In contrast, about one-third of oHSCs activate autophagy, control their metabolic activity, and are the fittest old stem cells that retain functional abilities in an adverse ageing bone marrow microenvironment. As all oHSCs remain competent for autophagy induction, it will be exciting to test whether rejuvenation interventions aimed at activating autophagy in unhealthy autophagy-inactivated oHSCs will improve the health of the ageing blood system.

© 2017 Macmillan Publishers Limited, part of Springer Nature. All rights reserved.